Volume 9
Number 6
14 February 2021
Pages 3079–3686

Journal of Materials Chemistry A

Materials for energy and sustainability

rsc.li/materials-a

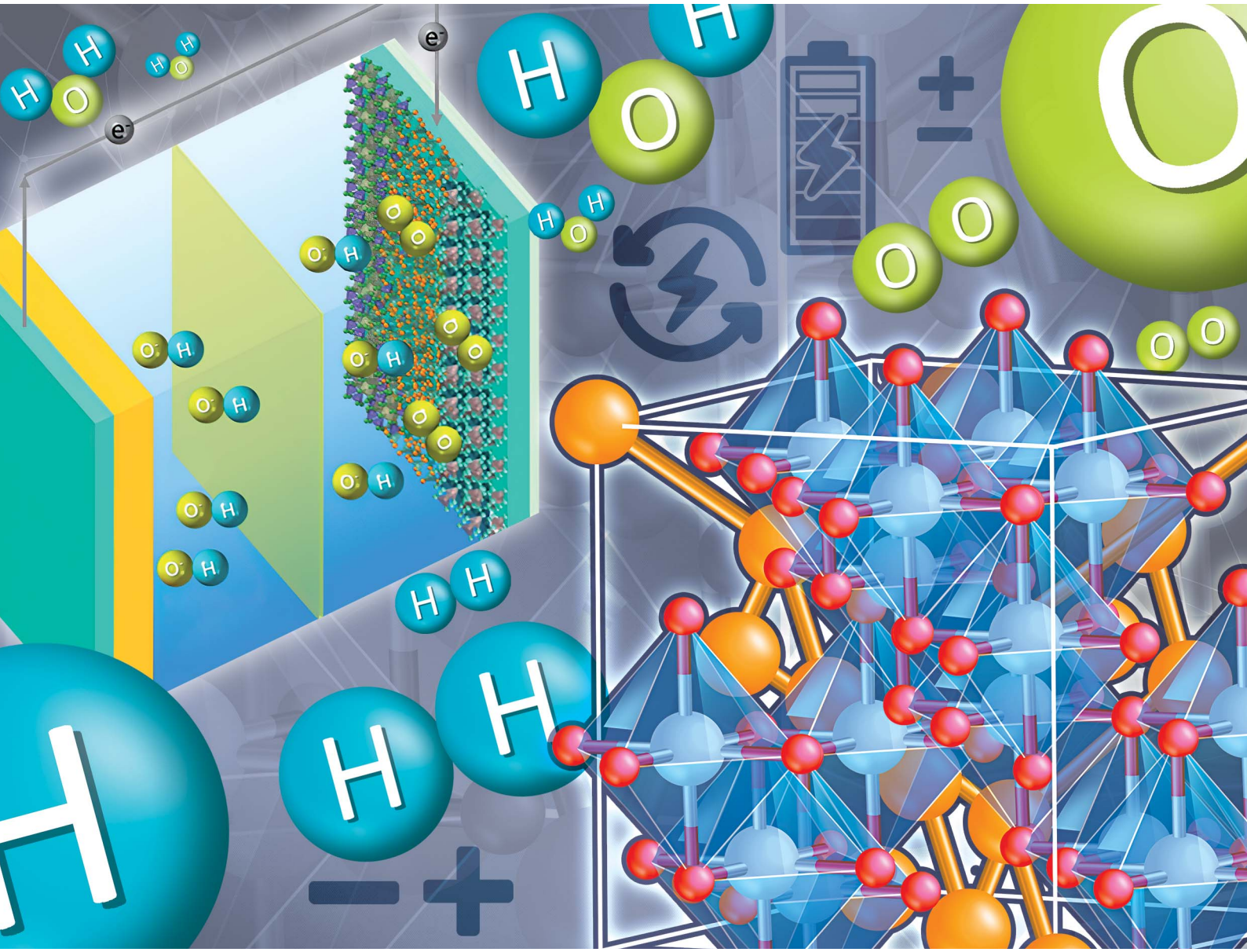

ISSN 2050-7488

ROYAL SOCIETY OF CHEMISTRY

REVIEW ARTICLE

Josué M. Gonçalves, Rodrigo A. A. Munoz, Chandra Sekhar Rout *et al.*

Multifunctional spinel $MnCo_2O_4$ based materials for energy storage and conversion: a review on emerging trends, recent developments and future perspectives

Journal of Materials Chemistry A

REVIEW

View Article Online
View Journal | View Issue

Cite this: J. Mater. Chem. A, 2021, 9, 3095

Multifunctional spinel $MnCo_2O_4$ based materials for energy storage and conversion: a review on emerging trends, recent developments and future perspectives

Josué M. Gonçalves, *[a] Murillo N. T. Silva,[b] Kusha Kumar Naik,[c] Paulo R. Martins,[e] Diego P. Rocha,[a] Edson Nossol,[b] Rodrigo A. A. Munoz,*[b] Lucio Angnes[a] and Chandra Sekhar Rout*[d]

The energy requirement of modern society increases every day. The depletion of the reserves of fossil fuel combined with the deleterious effects of CO_2 in the atmosphere is forcing all the world to search for alternative ways of generation and storing energy. Many scientists around the world are pursuing different forms to produce and store energy. Solar and wind sources are a reality for production of electricity, but are not continuous and require storage devices. The development of batteries and hybrid supercapacitors of high energy and power density is of great importance to complement this requirement of energy storage. Rechargeable metal–air batteries which utilize oxygen electrocatalysis seem to be an ideal choice, once the source of energy is not intermittent as solar and wind energy and is based on oxygen bifunctional electrocatalysis of both oxygen reduction and O_2 evolution reactions. In addition, water splitting allows the conversion and storage of solar/wind energy into chemical energy, generating fuels with high energy content. From this perspective, spinel $MnCo_2O_4$-based materials are promising structures for energy storage and conversion of energy. In this review, the use of low cost and abundant multifunctional materials for the development of supercapacitor devices and batteries was summarized. Completely, the design of electrocatalysts for water splitting and their capability to proportionate the tetra-electronic process of the oxygen reduction reaction are reviewed, including the main strategies in the preparation of these materials and considering their key multifunctional role in the way to a more sustainable society.

Received 15th November 2020
Accepted 8th December 2020

DOI: 10.1039/d0ta11129e

rsc.li/materials-a

[a]Instituto de Química, Universidade de São Paulo, Av. Prof. Lineu Prestes 748, 05508-000 São Paulo, SP, Brazil. E-mail: josuemartins@usp.br
[b]Instituto de Química, Universidade Federal de Uberlândia, Av. João Naves de Ávila 2121, Uberlândia, MG, 2121, Brazil. E-mail: munoz@ufu.br
[c]Department of Physics, Berhampur University, Odisha, India
[d]Centre for Nano and Material Sciences, Jain University, Jain Global Campus, Jakkasandra, Ramanagaram, Bangalore-562112, India. E-mail: r.chandrasekhar@jainuniversity.ac.in; csrout@gmail.com
[e]Instituto de Química, Universidade Federal de Goiás, Av. Esperança s/n, 74690-900 Goiânia, GO, Brazil

Josué Martins Gonçalves is a postdoctoral researcher in the group headed by Prof. Lucio Angnes at the University of Sao Paulo (USP), Brazil, and honored with a prestigious research fellowship from FAPESP. He graduated in Chemistry from University Vale do Acaraú (UVA) in 2014 and received his Ph.D. degree from USP in 2019, under the supervision of Prof. Koiti Araki. His current research interests include applications of nanomaterials in sensors, electrocatalysis and energy conversion and storage devices.

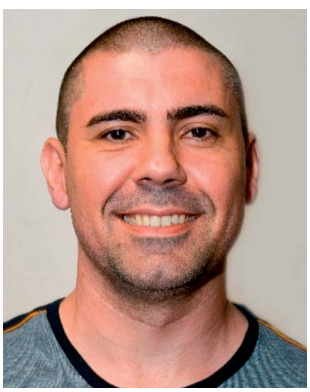

Paulo Roberto Martins received his Ph.D. degree from the Institute of Chemistry of University of Sao Paulo in 2012, under the guidance of Professor Koiti Araki. Currently, he is Assistant Professor at the Federal University of Goiás, Brazil. His research interests are focused on the development of new materials based on layered double hydroxides for energy storage purposes.

1. Introduction

With the increasing demand for environmentally friendly energy sources, alternatives have accelerated research on various renewable energy technologies such as fuel cells, metal–air batteries, and water-splitting devices as alternative energy production and storage systems.[1]

However, there are several scientific and technological challenges which require great efforts in the search for a more sustainable society. Among the main challenges, it is easy to identify the scientific race for low-cost and abundant materials for the command of the tetra-protonic and tetra-electronic reaction mechanism of the oxygen evolution reaction (OER),[2,3] a formidable challenge in the development of H_2 fuel cells. In addition, electrochemical oxygen reduction (ORR) and OER reactions are two key processes that limit the efficiency of important energy conversion devices such as metal–air batteries (MABs) and electrolytic cells.[4] On the other hand, the quest for much higher power and energy density devices, especially hybrid supercapacitors (HSCs), as alternatives to lithium-ion batteries (LIBs), has been the main objective of several research groups, as they can combine the outstanding power density of supercapacitive materials with the high energy density of battery-type materials into a single device.[5]

In this sense, researchers in materials science have strived to develop advanced and multifunctional materials for modern energy technologies, aiming to overcome the main challenges of energy conversion and storage. In fact, among the several recently studied materials, transition metal oxides (TMOs) have garnered attention due their high electronegativity, rich redox reactions and abundant density of active sites, low cost, environmental friendliness, and excellent electrochemical performance.[6] For instance, recently some review articles reported the use of Co_3O_4 and Co_3O_4-containing electrode materials for supercapacitors[7] and batteries.[8] In one of these recent

Diego Pessoa Rocha graduated in Chemistry in 2013, and received his Master's degree in Chemistry (2015) and Ph.D. (2020) from Federal University of Uberlândia, Brazil, under the guidance of Rodrigo A. A. Munoz, who is currently Associate Professor of Chemistry at the same university. He graduated in Chemistry in 2002 and obtained his Ph.D. in 2006 from the University of Sao Paulo Brazil. His current research interests focus on the development of novel electrochemical devices for (bio)sensors and electrocatalysis. He is an affiliate member of the Brazilian Academy of Science.

Edson Nossol received his Ph.D. degree from the Department of Chemistry of Federal University of Paraná in 2013. Currently, he is Adjunct Professor at the Federal University of Uberlândia, Brazil. His research interests are focused on the preparation of hexacyanoferrates/carbon nanostructures for application in sensors and energy storage devices.

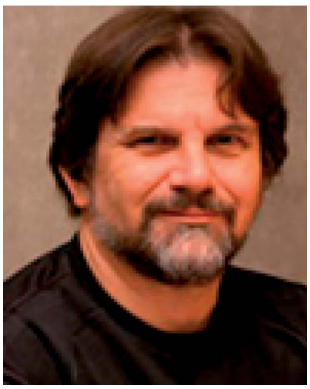

Lucio Angnes is full professor at the Institute of Chemistry of University of Sao Paulo. His research interests include the construction of electrodes with new and alternative materials, development of modified electrodes, design of arrays of microelectrodes, design of different procedures of enzyme immobilization (on electrodes or inside microchannels) and association of the created devices with flowing systems. He has authorized 160 research papers, is a member of the scientific board of Biosensors & Bioelectronics, Electroanalysis, and the Journal of Pharmaceutical Research and serves as Coordinator of Innovation at FAPESP (São Paulo State Research Foundation). He is a member of the Sao Paulo State Academy of Science.

Dr. Chandra Sekhar Rout is Associate Professor at Centre for Nano & Material Sciences, Jain University. Before joining CNMS, he was a DST-Ramanujan Fellow at I.I.T. Bhubaneswar, India (2013–2017). He received his B.Sc. (2001) and M.Sc. (2003) degrees from Utkal University and his Ph.D. from JNCASR, Bangalore (2008) under the supervision of Prof. C.N.R. Rao. He did his postdoctoral research at the National University of Singapore (2008–2009), Purdue University, USA (2010–2012) and UNIST, South Korea (2012–2013). His research interests include 2D materials for sensors, supercapacitors and energy storage devices, field emitters and electronic devices.

studies, Hu *et al.*[9] summarized the proposed strategies for improving specific capacitance, cycling stability, multifunctional capabilities of Co_3O_4 based materials and development prospects of Co_3O_4-based supercapacitor materials, providing a certain direction for application of Co_3O_4 in supercapacitors in the future. Complementarily, Shi and co-workers[8] discussed the synthesis and application of pure Co_3O_4 and its composites (Co_3O_4/C, Co_3O_4/graphene, Co_3O_4/metal oxide) in the field of LIBs. On the other hand, in the field of energy conversion, M. R. N. S. Hamdani, R. N. Singh, & P. Chartier (2010)[10] reviewed the performance of Co_3O_4 and Co-based spinel oxides as electrocatalysts for the OER or ORR.

Similar to Co_3O_4 and Co_3O_4-based materials, manganese-containing TMOs have also been intensively reported for applications in energy technologies,[6] especially those based on Mn_3O_4. For example, Zhu *et al.*[11] reviewed the electrochemical properties and reaction principles of Mn_3O_4-based composites with carbon and other metal compounds for supercapacitor electrodes. In addition to the use in supercapacitors, Ubale and colleagues[12] reported the main advances in the deposition, characterization, and applications of nanostructured manganese oxide thin films (NMOTFs) in LIBs, highlighting the structural and morphological studies. On the other hand, Tian and co-workers[13] reported the emerging applications of a series of MnO_x materials as highly efficient electrocatalysts for the OER, highlighting the reaction mechanisms, superiorities, and challenges of each type of MnO_x for future applications in the highly exciting energy-conversion-related areas.

As already mentioned in the studies cited above, spinel materials with a typical chemical formula of AB_2O_4 have been widely recognized and considered in the energy storage field,[14] and also as electrocatalysts in energy conversion devices. In fact, special attention has been given to spinel materials with bimetallic oxide structure, as they can result in materials with higher electrochemical activity, electrical conductivity, and more abundant redox reactions compared with monometallic oxides of A and B.[15] For example, some reviews reported the recent progress in the use of the $NiCo_2O_4$ spinel in supercapacitors,[16] batteries[17] and sensors.[18] More recently, Zhao *et al.*[14] summarized the main advances of 2D spinel structured Co-based MCo_2O_4 (M = Co, Ni, Zn, Cu, Fe, and Mn) materials as integrated electrodes for supercapacitor (SC) applications, detailing other different nanomaterials and 2D spinel structured Co-based materials for this application.

To our knowledge, more than five hundred articles report the preparation and/or use of the $MnCo_2O_4$ spinel for various applications, especially for energy conversion and storage. Thus, this compound has been widely recognized as a promising, versatile, and cost-efficiently bifunctional non-noble-metal electrocatalyst, due to its high redox stability, the complementation and synergy of both transition metals (manganese and cobalt), and efficient variable valence states.[19–22] As shown earlier, a few of the previous reviews have discussed the applications of Co_3O_4, Mn_3O_4 and $NiCo_2O_4$ spinels in energy storage, especially in supercapacitors and LIBs. However, as far as we know, there is no review work describing the promising results of $MnCo_2O_4$ in energy technologies. Therefore, in this review article we focus on the recent advances in $MnCo_2O_4$-based materials for energy applications and the main strategies used for the design of these materials (Scheme 1), including HSCs, LIBs and MABs, as well as the advancements achieved as electrocatalysts for water-splitting, more specifically for the hydrogen evolution reaction (HER) and OER. The pros and cons of using this spinel in the different devices are critically discussed. Finally, the evolving application of $MnCo_2O_4$ materials in the ORR is discussed, as well as the perspectives and future directions anticipated.

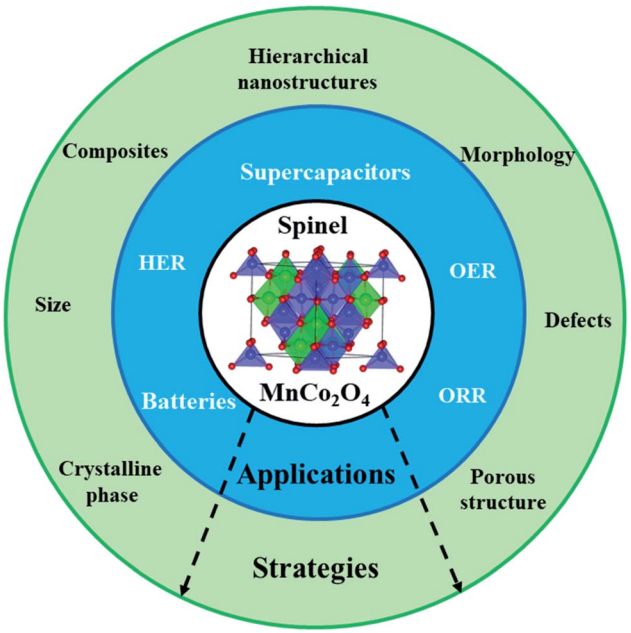

Scheme 1 Illustration of the strategies and applications of $MnCo_2O_4$ spinels. The atomic structure of the $MnCo_2O_4$ inverse spinel structure in the center of the scheme was reproduced with permission from ref. 23.

2. $MnCo_2O_4$ spinel: a supercapacitive or battery-type material?

The growing and fast demand for clean and sustainable energy storage devices has generated a scientific race for abundant and low-cost materials that can be used in high energy density devices, especially in high power density applications. However, this scientific race has also resulted in a great deal of confusion in the classification of supercapacitive and battery-like materials, especially in the distinction of "pseudocapacitive" and "battery" materials.[24] In this sense, several review articles have recently been published in order to alert the scientific community on these misunderstandings.

To clarify the confusion, Chodankar *et al.*[24] reported a review article that serves as a guide, providing the meanings and correct performance metrics of different electrode materials and using the electrochemical signatures and quantitative kinetics analysis as a method to distinguish battery-type and pseudocapacitive materials. For instance, electrical double-layer

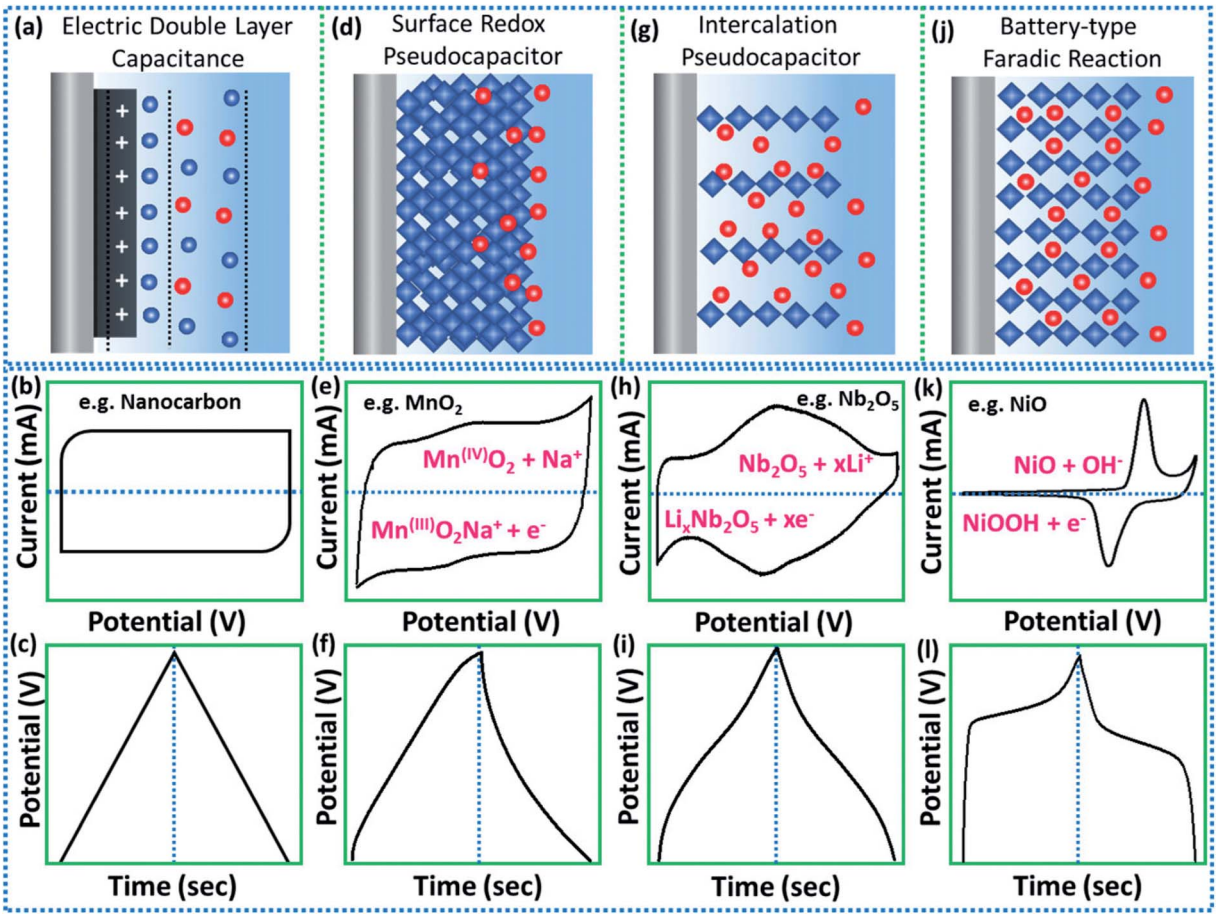

Fig. 1 The schematic illustration of the energy storage mechanisms with their corresponding electrochemical signatures (representative shapes of CV and CD curves): (a–c) electrical double layer capacitance, (d–f) surface redox capacitance, (g–i) intercalation capacitance, and (j–l) faradaic battery-type. Reproduced with permission from ref. 24. Copyright © 2020 Wiley-VCH GmbH.

capacitors (EDLCs) that store energy purely in the double-layer on a high surface area conductor[25] show a typical electrochemical signature of a supercapacitive material (Fig. 1a), that is, a rectangular cyclic voltammogram (CV, Fig. 1b) and galvanostatic charge/discharge (GCD) profile in the form of a symmetrical triangle (Fig. 1c). Similarly, pseudocapacitive materials have quasi-rectangular CVs and quasi-triangular GCD curves, however the charge storage mechanisms involve either (a) redox reactions at or near the surface (intrinsic pseudocapacitors); or (b) intercalation-type reactions.[24]

Surface-redox pseudocapacitors, for example, are well represented by ruthenium (RuO_2) and manganese oxides (MnO_2). In fact, due to their fast proton and electron-conducting properties at the surface of the electrode (Fig. 1d), their electrochemical signatures resemble those of EDLCs, as shown in Fig. 1e and f. In contrast, some layered oxides, such as Nb_2O_5 and MoO_3, can store energy by faradaic processes through the intercalation of electrolyte ions into the layers (Fig. 1g), especially in a nonaqueous electrolyte system, but without crystallographic phase changes. These materials are of the type "intercalation pseudocapacitors", but they should not be confused and called redox pseudocapacitors. According to Chodankar *et al.*,[24] a way to avoid this confusion is to carefully analyze the electrochemical features of intercalation pseudocapacitive materials and it was found that (i) they do not undergo phase transformations during intercalation, (ii) their peak potentials do not shift considerably with sweep rate, (iii) their current is linearly proportional to the sweep rate and (iv) their capacity does not vary significantly with charging time.

On the other hand, battery-type electrode materials have an electrochemical signature quite different from supercapacitive materials, since CVs display a couple of redox peaks (Fig. 1k) and plateau GCD profiles (Fig. 1l). This is due to the solid-state diffusion-controlled faradaic reactions characteristic of materials that present phase change of the electrode materials during the electrochemical process (Fig. 1j), such as oxides/hydroxides of Ni, Co, Cu, and Cd that react with hydroxide ions in alkaline media to store a charge.[24]

Then, is the $MnCo_2O_4$ spinel a supercapacitive or battery-type material? In the literature it is possible to find some studies that classify $MnCo_2O_4$ as a supercapacitive material, while others as battery-type. For example, V. Sannasi & K. Subbian[26] reported the preparation of high-pseudocapacitance $MnCo_2O_4$ nanostructures, while S. G. Krishnan, M. H. A. Rahim & R. Jose[27] reported the synthesis and characterization of $MnCo_2O_4$ cuboidal microcrystals as intercalation pseudocapacitors, however, both

studies presented the characteristic electrochemical signature of a battery-like material, such as CVs with a couple of redox peaks and plateau GCD profiles. In addition, peak potentials shifted considerably with sweep rate and capacity varied significantly with charging time. Thus, although many studies classify $MnCo_2O_4$ as a supercapacitive material, in this review work it was considered as a battery-type material, and in many cases the energy stored in the form of specific charge (C g^{-1}) was recalculated, since the average capacitance (F) was not constant throughout the potential window in the CVs.

In addition, it is also important to clarify that when assembling a battery-type electrode (ex.: $MnCo_2O_4$) with a supercapacitive-type electrode, a HSC is obtained, matching the advantages from both batteries and supercapacitors, and rendering them promising advanced energy storage devices for commercial applications.[28] In fact, experimental and theoretical studies[29] (shown below) demonstrated that $MnCo_2O_4$ has a superior electrical conductivity when compared to Co_3O_4, also showing greater storage capacity compared to other cobaltite spinels (MCo_2O_4; M = Ni,[28] Cu,[28] Zn[30] and Co[28,30]) with good cycling lifespan.[29] These characteristics demonstrate the promising possibilities of using these materials in high performance HSCs, as discussed below.

3. $MnCo_2O_4$-based materials for energy storage applications

3.1. Supercapacitors

3.1.1. Pristine $MnCo_2O_4$. Supercapacitors have received great attention owing to their high energy and power densities. Supercapacitors are highly desirable since this type of device can deliver high power and reasonable energy densities concurrently. Carbonaceous materials, conducting polymers and transition metal oxides have displayed higher energy density compared to other materials.[31–33] In particular, binary metal oxides have been considered for supercapacitor electrodes due to their high electrical conductivity relative to single component oxides and advantages of achievable mixed valences.[34] $MnCo_2O_4$ has attracted considerable interest in supercapacitor application since cobalt has a high oxidation potential, whereas manganese can have multiple oxidation states and exhibit higher capacity.[35]

In addition, it is important for a supercapacitor to have suitable fitting pore size distribution and large specific surface area, aiming to decrease the consumption of electrolyte by regulating the porous structure and morphology of the electrode, which determine the ion diffusion and conductivity, thereby affecting the capacitance of the supercapacitor. $MnCo_2O_4$ materials with different morphologies, such as spheres,[36] granules,[37] cuboidal microcrystals,[27] nanoneedles,[38] nanorods,[39,40] cubes,[26,41] nanosheets,[42–44] nanocages,[45] tunable porous structures,[46] hollow spheres,[47] and network-like porous structures,[48,49] can be prepared and tested for their usefulness as supercapacitor electrodes. For example, 1D $MnCo_2O_4$ nanowire arrays showed a specific capacitance of 349.8 F g^{-1} at 1 A g^{-1} and an energy density of 35.4 W h kg^{-1} at a power density of 225 W kg^{-1}.[50] Similarly, specific capacitances of 1342 F g^{-1} at 1 A g^{-1} and 988 F g^{-1} at 20 A g^{-1} were observed for $MnCo_2O_4$ nanowires synthesized by Xu *et al.*[51]

Liu *et al.*[29] reported a $MnCo_2O_4$ mesoporous nanowire array grown on nickel foam (NF) with a high specific capacitance. From Fig. 2a it is possible to observe that the nanowire has a mesoporous characteristic being formed by $MnCo_2O_4$ nanoparticles with a size distribution of ~20 nm (Fig. 2b) and a surface area of 98.5 m^2 g^{-1} (determined from N_2 isotherms). In order to figure out the effect of Mn on the $MnCo_2O_4$ spinel the projected density of states and electronic band structures were determined and the results are shown in Fig. 2c and d, respectively. Those studies demonstrated that $MnCo_2O_4$ has a superior electrical conductivity when compared to Co_3O_4. In fact, $MnCo_2O_4$ presented a valence bond very near the Fermi

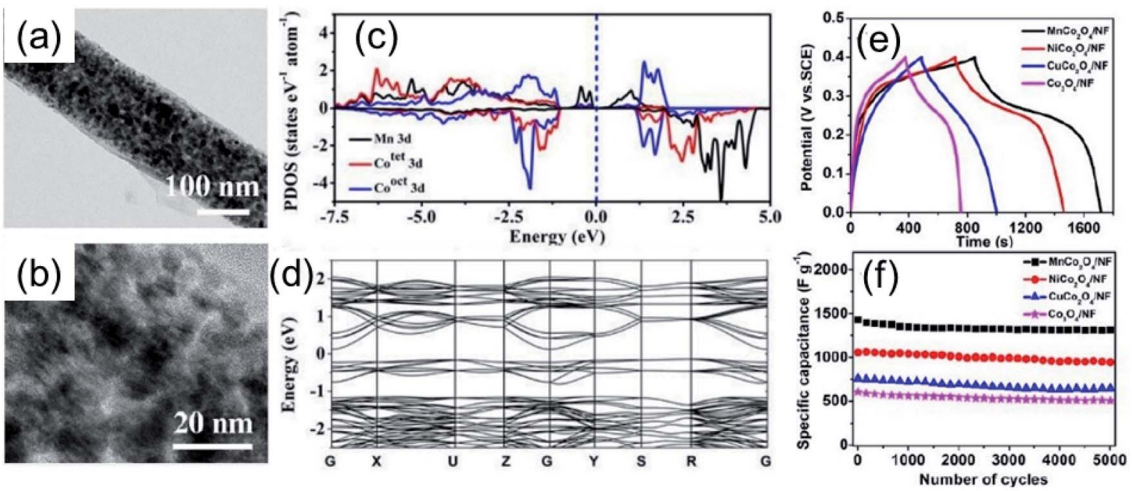

Fig. 2 TEM (a) and HRTEM (b) images of $MnCo_2O_4$ nanowires, (c and d) projected density of states and electronic band structures of $MnCo_2O_4$. (e) GCD curves of $MnCo_2O_4$ nanowires (black, at 1 A g^{-1}) and (f) cycling performance of $MnCo_2O_4$ nanowires (black, at 1 A g^{-1}). Reproduced with permission from ref. 29. Copyright © Marketplace™, Royal Society of Chemistry.

level and a low bandgap of 0.35 eV at the G point, in contrast the Co_3O_4 presented a bandgap of 1.72 eV at the same point. Also, the electrochemical behavior of $MnCo_2O_4$ nanowires was superior to that of Co_3O_4. A specific capacitance of 2146 F g^{-1} at a current density of 1 A g^{-1} was observed for $MnCo_2O_4$ nanowires, while for Co_3O_4 the specific capacitance was 948 F g^{-1},[29] Fig. 2e. In addition, the $MnCo_2O_4$ nanowires presented an excellent capacitance retention of 92.1% even after 5000 cycles of charge–discharge process, as can be seen in Fig. 2f.

3.1.2. $MnCo_2O_4$–metal oxide composite. The recent development of hierarchical nanostructures obtained using metal oxides directly grown on an active material (current collector) showed promising results.[52] These structures can be modulated in relation to their porosity and contact area between active materials and the electrolyte, providing more active sites in a given unit area without any auxiliary components, resulting in higher electrochemical properties. To link the performance gap between these materials, a variety of core–shell structure electrodes consisting of diverse compounds, such as Co_3O_4@-$MnCo_2O_4$,[53,54] $MnCo_2O_4$@$MnMoO_4$,[55] $MnCo_2O_4$@$NiMoO_4$,[56,57] and $MnCo_2O_4$@$CoMnO_4$ have been constructed so far which remarkably improved the electrochemical properties of these materials compared with the individual components. In this way, Shrestha *et al.*[58] reported a sandwich-type architecture of $MnCo_2O_4$@M-C@MnO_2 as an electrode material exhibiting an excellent areal/gravimetric capacity of 0.75 mA h cm^{-2}/ 312 mA h g^{-1} at 3 mA cm^{-2} with a capacity retention of 89.6% after 10 000 cycles. Besides, the hybrid supercapacitor presented an energy density of 68.2 W h kg^{-1} at 749.2 W kg^{-1} power density.

Liu *et al.*[59] reported the synthesis of a hierarchical $MnCo_2O_4$ nanowire@MnO_2 sheet core shell nanostructure showing an energy density of 85.7 W h kg^{-1} at a power density of 800 W kg^{-1}. Zheng and coauthors[60] also reported a hierarchical $MnCo_2O_4$@MnO_2 core–shell nanowire array exhibiting an energy density of 135.6 W h kg^{-1} at a power density of 513 W kg^{-1}.

Smarter integrated designs combined with different oxide materials are also reported, such as MnO_2,[61] CoO,[62] $NiWO_4$,[63] ZnO,[64] NiO,[65] $CoCo_2O_4$,[66] $CuCo_2O_4$,[67] $NiCo_2O_4$,[68] and $CoMnO_4$.[69] These types of structures possess many competitive advantages, including improvement of electrical conductivity, high electron aggregation efficiency, rich approachable electroactive sites, and even excellent synergetic effects or multifunctional properties of the nanostructure components.[70]

3.1.3. $MnCo_2O_4$-conducting polymer composites. Conducting polymers can store energy through rapid faradaic charge transfer, since the electrochemical process occurs both on the surface and interface of the electrode material (between the electrode and electrolyte), and due to this, they have been combined with $Mn_2Co_2O_4$ in the form of composites to increase the capacitance.[71] Conducting polymers with high electrical conductivity provide more active sites, which improve the maximum utilization of the $MnCo_2O_4$ electrode material. The $MnCo_2O_4$ nanoflakes@polypyrrole (PPy) nanowire electrode displayed a specific capacitance of 2933 F g^{-1} at 20 A g^{-1}.[32] Similarly, Wang *et al.*[72] reported the preparation of $MnCo_2O_4$@PPy nanostructures on graphite foam (GNF), as described in Fig. 3a. The $MnCo_2O_4$@PPy/GNF was prepared in different concentrations of PPy, being denoted as $MnCo_2O_4$@-PPy/GNF-*n*, where *n* was varied from 1 to 6 and the SEM images are shown in Fig. 3b–g. It is possible to observe that PPy grows vertically on $MnCo_2O_4$ as the concentration of PPy increases, thus forming interconnected network nanosheets. The $MnCo_2O_4$@PPy/GNF-5 exhibited a specific capacitance of 2364 F g^{-1} and a rate capability of 55.2% from 1 to 50 A g^{-1}.

Furthermore, a HSC was built with $MnCo_2O_4$@PPy/GNF-5 and activated microwave exfoliated graphite oxide (a-MEGO) as positive and negative electrodes, respectively. The HSC showed an energy density of 25.7 W h kg^{-1} and a power density of 16.1 kW kg^{-1}, besides a capacitance retention of 85.5% after incredible 10 000 cycles (Fig. 3h). Hu *et al.*[73] also reported a composite based on PPy decorated by $MnCo_2O_4$ urchins showing an energy density of 0.785 mW h cm^{-1} at a power density of 7.49 W cm^{-1} as the positive electrode for supercapacitors.

3.1.4. $MnCo_2O_4$–carbon based composites. Materials based on carbon structures have a large specific surface area, good electrical conductivity and strong mechanical strength, thus becoming leading materials for the electrodes applied for supercapacitors. However, the specific capacitance of carbon is much lower than that of transition metal oxides, which limits their practical applications to a certain degree. Fortunately, carbon modifications can improve the electrical conductivity of $MnCo_2O_4$-based electrode materials.[74,75] Moreover, the combined effects of $MnCo_2O_4$ structure with different materials of conducting carbons, such as graphene,[31,33,76,77] activated carbon,[78,79] carbon nanofibers,[80] carbon aerogels,[81] reduced graphene oxide (rGO),[82,83] carbon nanotubes (CNTs), and graphene quantum dots,[84] are very promising to improve the overall performance of the system. In this way, Saren *et al.*[85] reported the preparation of flower-like hybrid spinel $MnCo_2O_4$@graphene nanosheets and $MnCo_2O_4$@CNT nanocomposites by a hydrothermal method for supercapacitor application. A specific capacitance of 923.97 F g^{-1}, an energy density of 82.13 W h kg^{-1} and a power density of 399.74 W kg^{-1} at a current density of 1 A g^{-1} were observed for $MnCo_2O_4$@-graphene nanosheets, while a specific capacitance of 579.71 F g^{-1} was achieved for $MnCo_2O_4$@CNT.

Wu and coworkers[77] developed a new bifunctional composite based on $MnCo_2O_4$/nanographene (B-n-$MnCo_2O_4$) prepared on a macroporous electrically conductive network (MECN) as an electrode material for supercapacitors and sodium ion batteries. The 3D structure of nanographene coating MECN and B-n-$MnCo_2O_4$@MECN can be seen in Fig. 3i–l. Fig. 3i and k show nanographene layers with a lateral size of 50–200 nm and when the B-*n*-$MnCo_2O_4$ was incorporated onto the MECN (Fig. 3j and l) the 3D nanostructure displayed a uniform diameter of ~50 nm. This 3D interconnected morphology seems to be very interesting since it can improve the electronic conductivity, in addition to facilitating electrochemical reactions, because of its large surface area. The B-n-$MnCo_2O_4$@-MECN presented a high specific capacitance of 7.02 F cm^{-2} (2341 F g^{-1}) at 3 mA cm^{-2}. The specific capacitance of B-n-

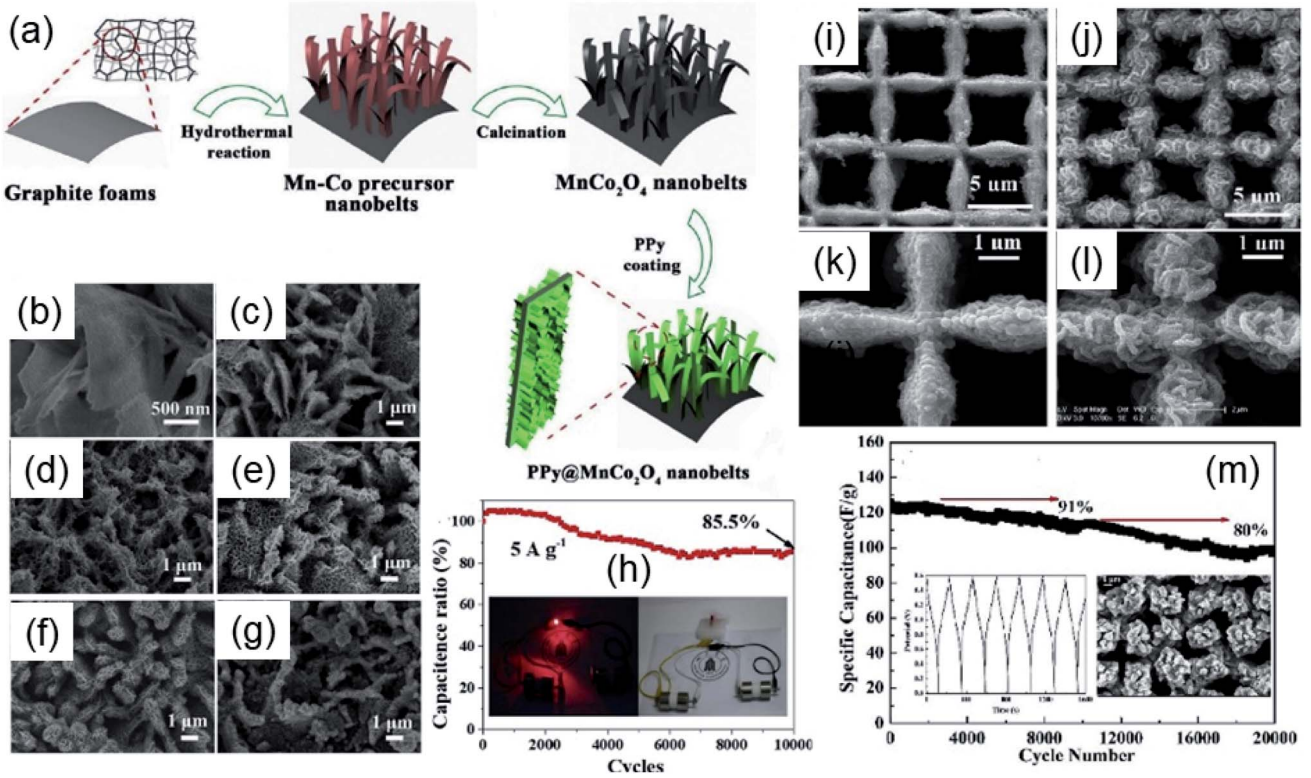

Fig. 3 Scheme of the synthesis process of PPy@$MnCo_2O_4$/GNF (a), SEM images of the PPy@$MnCo_2O_4$/GNF-*n* (*n* = 1–6) (b–g) and cycling stability performance of the hybrid supercapacitor PPy@$MnCo_2O_4$/GNF-5//a-MEGO (h). Reproduced with permission from ref. 72. Copyright © 2018 Elsevier B.V. All rights reserved. SEM images of nanographene@MECN at low (i) and high magnification (k) and B-n-$MnCo_2O_4$@MECN at low (j) and high magnification (l). Stability electrochemical performance of the hybrid supercapacitor B-n-$MnCo_2O_4$@MECN//AC@Ni foam (m). Reproduced with permission from ref. 77. Copyright © 2020 Elsevier B.V. All rights reserved.

$MnCo_2O_4$@MECN is much larger than that of Mn_3O_4/nanographene@MECN (2.7 F cm^{-2}) and Co_3O_4/nanographene@MECN (2.2 F cm^{-2}) at the same current density, which highlights the presence of $MnCo_2O_4$ in the composite.

Also, a HSC was built with B-n-$MnCo_2O_4$@MECN and AC@Ni foam as positive and negative electrodes, respectively. The device provided an outstanding long lifetime and stability as well. Even after incredible 20 000 charge–discharge cycles the device showed a capacitance retention of 80%, as can be seen in Fig. 3m. The long lifetime can be attributed to good adhesion between all the components and good electrical contact between B-n-$MnCo_2O_4$ and MECN as the current collector.

3.1.5. Other $MnCo_2O_4$-based composite materials. $MnCo_2O_4$@CoS,[86] $MnCo_2O_4$/Ni,[87,88] $MnCo_2O_4$@nitrogen-doped carbon,[89] $MnCo_2O_4$/Ni/Cu,[90] $MnCo_2O_4$@$Co(OH)_2$,[91] and $MnCo_2O_4$@$Ni(OH)_2$ belts[92] are also introduced as positive electrodes for supercapacitor applications, which delivered capacitances comparable with those of the previously discussed composites. For example, Lv *et al.*[93] reported a novel self-supported $MnCo_2O_4$@Ni_3S_2 core–shell heterostructure, showing a specific capacitance of 2807 F g^{-1} at 3 A g^{-1}. The same research group[94] also described a hierarchical $MnCo_2O_4$/NiMn composite deposited on Ni foam. The layer-by-layer architecture combined with the synergistic effect of both components of the composite provided a specific capacitance of 3063 F g^{-1} at 3 A g^{-1} and a cycle stability of 94.7% at 20 A g^{-1} over 5000 cycles.

Most of the materials previously-mentioned were deposited on Ni foam as the conductive substrate,[27,57,60,65] which did not require the addition of polymer binders, and promoted rapid electron transport between the active material and current collector, thereby resulting in a substantially efficient substrate, due to the high electrical conductivity (1.43 × 10^7 Ω^{-1}) and thermal conductivity (90.7 W mK^{-1}) of Ni.[90] Nevertheless, other conductive substrates and current collectors have also been employed, such as carbon aerogels,[81] graphite foam,[72] indium-doped tin oxide,[44] activated carbon,[78] microporous electrically conductive networks,[77] graphite paper,[59,67,95] carbon fiber paper[96] and copper foil.[35] Table 1 presents the performance of different supercapacitor materials coupled with different types of electrodes based on $MnCo_2O_4$.

3.2. Batteries

3.2.1. Lithium-ion batteries. Rechargeable Li-ion batteries (LIBs) were shown as the most efficient energy storage devices, since the small size of lithium ions makes their diffusion more favorable in a variety of structures.[103] Spinel binary transition-metal oxide materials, such as $MnCo_2O_4$, have been widely investigated as anode electrodes for LIBs, due to their lower cost and better electronic conductivity than single-metal oxides.[104,105]

Table 1 Performances of some reported $MnCo_2O_4$-based supercapacitors[a]

Type	Material	Specific capacitance (F g^{-1})	Specific capacity (C g^{-1})	Potential window (V *vs.*)	Retention (%), rate capability (A g^{-1})	Cycling stability	Highest energy density (W h kg^{-1})	Highest power density: (kW kg^{-1})	Negative electrode material	Ref.
Pristine	Flake-like $MnCo_2O_4$	1487 F g^{-1} at 1 A g^{-1}	594.8 C g^{-1}	0.0–0.4 V (*vs.* SCE)	—	93.3% (2000 cycles)	—	—	—	35
	$MnCo_2O_4$	405 F g^{-1} at 1 mA cm^{-2}	—	0–0.4 V (*vs.* SCE)	67.9%, (5–40 mA cm^{-2})	95.1% (1000 cycles)	—	—	—	37
	$MnCo_2O_4$ nanorods	845 F g^{-1} at 1 A g^{-1}	422.5 C g^{-1}	0.0–0.5 V (*vs.* Hg/HgO)	51.6%, (1–20 A g^{-1})	90.2% (2000 cycles)	53.7	8	rGO/NF	39
	$MnCo_2O_4$ nanorods	718.75 F g^{-1} at 0.5 A g^{-1}	287.5 C g^{-1}	0.0–0.4 V (*vs.* Ag/AgCl)	—	100% (1000 cycles)	—	—	—	40
	$MnCo_2O_4$ hollow spheres	0.8 F cm^{-2} at 2 mA cm^{-2}	0.32 C cm^{-2}	0.0–0.4 V (*vs.* SCE)	—	99% (2000 cycles)	0.052 mW h cm^{-3}	320 mW cm^{-3}	AC/CFs	47
	Porous sphere $MnCO_2O_4$	1044 F g^{-1} at 0.5 A g^{-1}	574.2 C g^{-1}	0.0–0.55 V (*vs.* Hg/HgO)	68.9%, (1–20 A g^{-1})	133.3% (10 000 cycles)	42.27	0.4	Starch-derived carbon foam	36
	Network-like porous $MnCo_2O_4$	647.42 F g^{-1} at 1 A g^{-1}	323.71 C g^{-1}	0.1–0.6 V (*vs.* Hg/HgO)	70.67%, (1–10 A g^{-1})	93.68% (3000 cycles)	—	—	—	48
	$MnCO_2O_4$ nanowires	2146 F g^{-1} at 1 A g^{-1}	858.4 C g^{-1}	0.0–0.4 V (*vs.* SCE)	—	92.1% (5000 cycles)	29.3	8	AC	29
	$MnCO_2O_4$ nanowires	405 F g^{-1} at 1 A g^{-1}	202.5 C g^{-1}	0.0–0.5 V (*vs.* Hg/HgO)	51.4%, (1–10 A g^{-1})	91% (4000 cycles)	—	—	—	97
	$MnCO_2O_4$ nanowires	1342 F g^{-1} at 1 A g^{-1}	738.1 C g^{-1}	0.0–0.55 V (*vs.* Hg/HgO)	73.6%, (1–20 A g^{-1})	—	—	—	—	51
	$MnCO_2O_4$ nanowires	349.8 F g^{-1} at 1 mV s^{-1}	157.4 C g^{-1}	0.0–0.45 V (*vs.* Ag/AgCl)	94%, (1–20 A g^{-1})	94% (4000 cycles)	33.3	4.5	—	50
	$MnCo_2O_4$ nanoparticles	1068.5 F g^{-1} at 1 A g^{-1}	427.2 C g^{-1}	0.0–0.4 V (*vs.* SCE)	50%, (1–8 A g^{-1})	90% (2000 cycles)	—	—	—	26
	Chestnut-like $MnCo_2O_4$ nanoneedles	1535 F g^{-1} at 1 A g^{-1}	921 C g^{-1}	0.0–0.6 V (*vs.* SCE)	61.8%, (1–10 A g^{-1})	94.3% (12 000 cycles)	~60.4	~0.375	Graphene/NF	38
	$MnCo_2O_4$ nanosheets	2000 F g^{-1} at 0.5 A g^{-1}	1000 C g^{-1}	0.0–0.5 V (*vs.* Hg/HgO)	57.5%, (0.5–20 A g^{-1})	92.3% (5000 cycles)	73.95	15	rGO	42
	Nanocage $MnCo_2O_4$	1763 F g^{-1} at 1 A g^{-1}	969.65 C g^{-1}	0.0–0.55 V (*vs.* Hg/HgO)	—	95% (4500 cycles)	54.15	0.324	Nanocage $MnCo_2O_4$	45
	Flower-like $MnCo_2O_4$	249.3 F g^{-1} at 0.5 A g^{-1}	174.5 C g^{-1}	−0.3–0.4 V (*vs.* Hg/HgO)	78.8%, (0.5–5 A g^{-1})	93.6% (2000 cycles)	—	—	—	98
	Flower-like $MnCo_2O_4$	571 F g^{-1} at 0.5 A g^{-1}	285.5 C g^{-1}	−0.1–0.4 V (*vs.* Hg/HgO)	87.7%, (0.5–5 A g^{-1})	96.1% (2000 cycles)	—	—	—	99
	$MnCo_2O_4$ cubes	480.5 F g^{-1} at 1 A g^{-1}	264.3 C g^{-1}	0.0–0.55 V (*vs.* Hg/HgO)	75.7%, (1–25 A g^{-1})	96.6% (3000 cycles)	—	—	—	41
	$MnCo_2O_4$ cuboidal microcrystals	600 F g^{-1} at 0.5 A g^{-1}	300 C g^{-1}	0.0–0.5 V (*vs.* Ag/AgCl)	55.7%, (0.5–5 A g^{-1})	132% (3000 cycles)	—	—	—	27
	$MnCo_2O_4$	270 F g^{-1} at 10 mV s^{-1}	—	−1.2–1.5 V (*vs.* Ag/AgCl)	—	92.4% (1000 cycles)	14.85	0.495	—	49

Table 1 (*Contd.*)

Type	Material	Specific capacitance (F g^{-1})	Specific capacity (C g^{-1})	Potential window (V *vs.*)	Retention (%), rate capability (A g^{-1})	Cycling stability	Highest energy density (W h kg^{-1})	Highest power density: (kW kg^{-1})	Negative electrode material	Ref.
	Porous $MnCo_2O_4$	151 F g^{-1} at 5 mV s^{-1}	—	0–0.5 V (*vs.* SCE)	83.6%, (0.1–5 A g^{-1})	—	—	—	—	95
	$MnCo_2O_4$ nanosheets	—	282 C g^{-1} at 1 A g^{-1}	0–0.55 V (*vs.* SCE)	25.2%, (1–10 A g^{-1})	84% (1500 cycles)	2.55	37.57	$FeMn_2O_4$	43
	$MnCo_2O_4$ nanorods	187.0 F g^{-1} at 0.25 A g^{-1}	51.9 C g^{-1}	0.0–0.4 V (*vs.* Ag/AgCl)	8%, (0.25–30 A g^{-1})	90% (2000 cycles)	12.77	2.520	AC	100
	$MnCo_2O_4$ nanosheets	250 F g^{-1} at 0.25 A g^{-1}	100 C g^{-1}	0.0–0.4 V (*vs.* Ag/AgCl)	10.8%, (0.25–10 A g^{-1})	95% (1000 cycles)	10.04	5.2	—	44
$MnCo_2O_4$-metal oxide	Co_3O_4@$MnCo_2O_4$	736.5 F g^{-1} at 1 mA cm^{-2}	—	0–0.5 V (*vs.* SCE)	—	79.95% (3000 cycles)	—	—	—	53
	$MnCo_2O_4$@Co_3O_4	—	1440 C cm^{-2} at 1 mA cm^{-2}	0.0–0.45 V (*vs.* SCE)	—	101.23% (8000 cycles)	31	0.208	AC	54
	$MnCo_2O_4$@$CoMnO_4$	2115.38 F g^{-1} at 1.1 A g^{-1}	1100 C g^{-1}	0.0–0.52 V (*vs.* Hg/HgO)	47.4%, (1.1–6.6 A g^{-1})	119% (5000 cycles)	37.5	0.527	AC	69
	$MnCo_2O_4$@$CoCo_2O_4$	614 F g^{-1} at 1 A g^{-1}	276.3 C g^{-1}	0.0–0.45 V (*vs.* SCE)	76.9%, (1–10 A g^{-1})	77.5% (5000 cycles)	—	—	—	66
	$MnCo_2O_4$@$NiMoO_4$	1718 F g^{-1} at 1 A g^{-1}	859 C g^{-1}	0.0–0.5 V (*vs.* Hg/HgO)	69.8%, (1–8 A g^{-1})	84% (6000 cycles)	42.3	0.797	AC	56
	$CuCo_2O_4$/$MnCo_2O_4$	1434 F g^{-1} at 0.5 A g^{-1}	860.4 C g^{-1}	0.0–0.6 V (*vs.* SCE)	56.6%, (0.5–15 A g^{-1})	81.4% (5000 cycles)	42.1	0.4	Graphene/NF	67
	$MnCo_2O_4$@$NiMoO_4$	1244 F g^{-1} at 1 A g^{-1}	746.4 C g^{-1}	0.0–0.6 V (*vs.* SCE)	91%, (1–10 A g^{-1})	81% (2500 cycles)	42	0.8	AC	57
	$NiCo_2O_4$–$MnCo_2O_4$	1152 F g^{-1} at 1 A g^{-1}	576 C g^{-1}	0.0–0.5 V (*vs.* Ag/AgCl)	72.2%, (1–10 A g^{-1})	95.4% (3000 cycles)	40	0.2	—	68
	MnO_2/$MnCO_2O_4$	497 F g^{-1} at 0.5 A g^{-1}	248.5 C g^{-1}	0.0–0.5 V (*vs.* Hg/HgO)	62.8%, (0.5–10 A g^{-1})	60% (5000 cycles)	—	—	—	61
	$MnCo_2O_4$@NiO	508.3 F g^{-1} at 2 A g^{-1}	279.6 C g^{-1}	0.0–0.55 V	67.7%, (0.5–6 A g^{-1})	89.7% (2000 cycles)	—	—	—	65
	$MnCo_2O_4$@$NiWO_4$	5.09 F cm^{-2} at 1 mA cm^{-2}	2.54 C cm^{-2}	0.0–0.5 V (*vs.* Hg/HgO)	26.1%, (1–20 mA cm^{-2})	96% (5000 cycles)	0.23 mW h cm^{-2}	2.66 mW cm^{-2}	AC	63
	CoO/MnO_2/$MnCO_2O_4$ composite nanowires	1650 F g^{-1} at 1 A g^{-1}	660 C g^{-1}	0.0–0.4 V (*vs.* Ag/AgCl)	60.0%, (1–15 A g^{-1})	—	90	10	CoO/MnO_2/$MnCO_2O_4$ composite nanowires	62
	r$MnCo_2O_4$@rMnO_2	3.39 F cm^{-2} at 3 mA cm^{-2}	0.4 mA h cm^{-2}	0.0–0.4 V (*vs.* SCE)	48.9%, (3–60 mA cm^{-2})	92.5% (3000 cycles)	32.4	4.524	AC	101
	$MnCo_2O_4$@MnO_2 core–shell arrays	2262 F g^{-1} at 1 A g^{-1}	904.8 C g^{-1}	0.0–0.4 V (*vs.* SCE)	48.8%, (1–20 A g^{-1})	87.1% (5000 cycles)	34.7	24	Graphene/NF	59
	ZnO@$MnCo_2O_4$	631.2 F g^{-1} at 1 A g^{-1}	504.9 C g^{-1}	−0.2–0.6 V (*vs.* SCE)	31.7%, (1–10 A g^{-1})	92.3% (1000 cycles)	56.10	0.4	—	64
	$NiCo_2O_4$–$MnCo_2O_4$ rose-like composite	1100 F g^{-1} at 1 A g^{-1}	440 C g^{-1}	0.0–0.4 V (*vs.* SCE)	69.1%, (1–10 A g^{-1})	—	—	—	—	102

Table 1 (*Contd.*)

Type	Material	Specific capacitance (F g^{-1})	Specific capacity (C g^{-1})	Potential window (V *vs.*)	Retention (%), rate capability (A g^{-1})	Cycling stability	Highest energy density (W h kg^{-1})	Highest power density: (kW kg^{-1})	Negative electrode material	Ref.
	$MnCo_2O_4$@$MnMoO_4$ core–shell	—	885 C g^{-1} at 3 A g^{-1}	0.0–0.4 V (*vs.* SCE)	71%, (3–30 A g^{-1})	95% (5000 cycles)	49.4	0.815	AC	55
$MnCo_2O_4$-conducting polymer	$MnCo_2O_4$@PPy/GNF	2933 F g^{-1} at 2 A g^{-1}	1466.5 C g^{-1}	0.0–0.5 V (*vs.* Ag/AgCl)	55.3%, (2–20 A g^{-1})	86.7% (5000 cycles)	78.2	1.121	AC	32
	$MnCo_2O_4$@PPy	—	2.862 mA h cm^{-2} at 1 mA cm^{-2}	0.0–0.5 V (*vs.* Hg/HgO)	84.5%, (1–10 mA cm^{-2})	88% (2000 cycles)	0.785 mW h cm^{-3}	7.49 mW cm^{-3}	AC	73
	Polypyrrole@$MnCo_2O_4$/graphite foam	2364 F g^{-1} at 1 A g^{-1}	1182 C g^{-1}	−0.1–0.4 V (*vs.* Ag/AgCl)	55.2%, (1 to 50 A g^{-1})	85.3% (1000 cycles)	25.7	16.1	a-MEGO	72
$MnCo_2O_4$-carbon based composites	$MnCo_2O_4$/graphene	503 F g^{-1} at 1 A g^{-1}	201.2 C g^{-1}	0.0–0.4 V (*vs.* SCE)	65.5%, (1–20 A g^{-1})	97.4% (5000 cycles)	—	—	—	76
	Flower-like $MnCo_2O_4$/rGO	923.97 F g^{-1} at 1 A g^{-1}	739.2 C g^{-1}	0.0–0.8 V (*vs.* Ag/AgCl)	—	111% (5000 cycles)	82.13	0.399	Carbon black	85
	$MnCo_2O_4$@nitrogen doped graphene@ MnO_2	1170 F g^{-1} at 1 A g^{-1}	585 C g^{-1}	0.0–0.5 V (*vs.* Ag/AgCl)	69.9%, (1–20 A g^{-1})	87.6% (5000 cycles)	48.5	∼0.808	Nitrogen doped graphene hydrogel	33
	C@$MnCo_2O_4$	728.4 F g^{-1} at 1 A g^{-1}	364.2 C g^{-1}	0.0–0.5 V (*vs.* Ag/AgCl)	71.3%, (1–10 A g^{-1})	—	25.5	0.856	—	79
	$MnCo_2O_4$@activated carbon	—	443.5 C g^{-1} at 0.5 A g^{-1}	−1.0–0.4 V (*vs.* SCE)	—	66.95% (5000 cycles)	—	—	—	78
	$MnCo_2O_4$ graphene quantum dots	1625 F g^{-1} at 1 A g^{-1}	812.5 C g^{-1}	0.0–0.5 V (*vs.* Hg/HgO)	80%, (0.5–10 A g^{-1})	80% (5000 cycles)	46	0.066	rGO	84
	B-n-$MnCo_2O_4$@MECN	7.02 F cm^{-2} at 3 mA cm^{-2}	—	−0.1–0.45 V (*vs.* Hg/HgO)	31%, (3–20 mA cm^{-2})	98% (5000 cycles)	50.5	6.4	AC/NF	77
Other $MnCo_2O_4$-based composite materials	$MnCo_2O_4$@$Co(OH)_2$		1185 C g^{-1} at 1 A g^{-1}	0–0.5 V (*vs.* SCE)	78%, (1–20 A g^{-1})	96% (5000 cycles)	67.2	0.8	N-CNTs@rGO	91
	$MnCo_2O_4$@$Ni(OH)_2$	2154 F g^{-1} at 5 A g^{-1}	969.3 C g^{-1}	0.0–0.45 V (*vs.* SCE)	32.6%, (5–20 A g^{-1})	90% (2500 cycles)	48	14.9	$MnCo_2O_4$@$Ni(OH)_2$	92
	$MnCo_2O_4$@Ni_3S_2 core–shell heterostructures	2807 F g^{-1} at 3 A g^{-1}	1122.8 C g^{-1}	0.0–0.4 V (*vs.* SCE)	69.0%, (3–30 A g^{-1})	92% (5000 cycles)	—	—	—	93
	$MnCo_2O_4$@NiMn	3063 F g^{-1} at 3 A g^{-1}	1378.3 C g^{-1}	0.0–0.45 V (*vs.* SCE)	75.6%, (3–30 A g^{-1})	94.7% (5000 cycles)	51.9	0.8	AC	94
	Dual-$MnCo_2O_4$/Ni	2265 F g^{-1} at 1.7 A g^{-1}	283 mA h g^{-1}	0–0.45 V (*vs.* Ag/AgCl)	70%, (2–10 mA cm^{-2})	85% (2000 cycles)	—	—	—	88
	$MnCo_2O_4$@CoS	1607.4 F g^{-1} at 0.8 A g^{-1}	723.3 C g^{-1}	0.0–0.45 V (*vs.* SCE)	—	91.5% (5000 cycles)	55.1	0.477	AC	86

[a] AC = activated carbon; a-MEGO = activated microwave exfoliated graphite oxide; CFs = carbon fibres; rGO = reduced graphene oxide; NF = nickel foam; N-CNTs = N-doped carbon nanotubes; PPy = polypyrrole; r$MnCo_2O_4$@rMnO_2 = reduced core–shell structured $MnCo_2O_4$@MnO_2. * By cyclic voltammetry.

A large variety of nanoscale building blocks of $MnCo_2O_4$ have been widely investigated, especially due to their good electrochemical performance.[106]

In order to improve the electrochemical performance of $MnCo_2O_4$ structures as anodic materials in LIBs, morphological modifications and synthesis methods have been the focus of investigations.[107–113] One of these strategies has been focused on the preparation of porous $MnCo_2O_4$ materials[114,115] and on the development of diverse substrates as current collectors (carbon cloth,[116–118] Ni foam[113] and copper foil[115,119]) with robust adhesion to obtain a binder-free anode material. Li *et al.*[120] first developed a two-step method to prepare uniform hollow $MnCo_2O_4$ submicrospheres with multilevel interiors (mesoporous, hollow, yolk–shell, shell-in-shell, and yolk-in-double-shell spheres). The yolk–shell morphology (Fig. 4a) showed the best performance among these multilevel interior structures, with an initial discharge capacity of 1425 mA h g^{-1} at a current density of 400 mA g^{-1} (Fig. 4b). Huang *et al.*[121] also fabricated spherical yolk–shell $MnCo_2O_4$ powders (Fig. 4c) by a hydrothermal method followed by a thermal treatment, with an initial discharge capacity of 1445 mA h g^{-1} at 0.2 A g^{-1} and capacity retention of ~860.0 mA h g^{-1} after 40 cycles at 0.2 A g^{-1} (Fig. 4d). The literature reports the preparation of different $MnCo_2O_4$ porous based structures for anode electrodes, such as spheres,[122,123] yolk–shell microspheres[124] (Fig. 4e and f), microflowers,[125] hydrangea-like structures,[126] and dumbbell-shaped structures.[127]

Fu *et al.*[106] reported the preparation of microspheres of $MnCo_2O_4$ by a calcination-free method; in this work, two kinds of $MnCo_2O_4$ crystals with different exposed facets of $(\bar{1}\bar{1}0)$ and $(1\bar{1}\bar{2})$ were synthesized, presenting two different morphologies, particle-assembled and sheet-assembled microspheres, respectively. The anode was evaluated, and the microspheres delivered a capacity of 722 mA h g^{-1} after 25 cycles at a current density of 200 mA g^{-1}, and capacities up to 553 and 320 mA h g^{-1} after 200 cycles at a current density of 400 and 900 mA g^{-1}, respectively.

Huang and colleagues[128] proposed a novel core–shell ellipsoidal $MnCo_2O_4$ powder with a desired micro-/nano-structure and unique concentration gradient. The battery tests demonstrated excellent values of initial discharge capacities (1433.3 mA h g^{-1} at 0.1 A g^{-1} and 1248.4 mA h g^{-1} at 0.4 A g^{-1}), capacity retention (~900.0 mA h g^{-1} after 60 cycles at 0.1 A g^{-1}) and rate performance (~620.0 mA h g^{-1} after 50 cycles at 0.4 A g^{-1}).

Developing composites of $MnCo_2O_4$ with other materials is an important strategy to improve the performance of LIBs.[129,130] A 3D sandwich-shape graphene based nanocomposite intercalated with double-shelled hollow $MnCo_2O_4$ spheres as an anode material for LIBs has been synthesized, showing a rate capability of 538 mA h g^{-1} at a current density of 1000 mA g^{-1} and outstanding cycle performance, with a capability of 703 mA h g^{-1} after 100 cycles at 200 mA g^{-1}.[131] The literature also reports the synthesis of $MnCo_2O_4$ containing nickel,[132,133] Co_3O_4,[119] CoO,[118] MnO_2,[134] TiO_2,[135] and $NiCo_2O_4$.[102] Huang and coauthors[136] designed a $MnCo_2O_4$@N-doped carbon@MnO_2 three layered core shell octahedron as an anode material for Li-ion storage, which displayed a discharge capacity of 894 mA h g^{-1} at a current density of 500 mA g^{-1} after 120 cycles. Even at a high current density of 1000 mA g^{-1}, the discharge capacity remained at 839 mA h g^{-1} after 600 cycles.

Some conductive substrates have also served as current collectors to further improve the electrochemical performance of electrode materials, including carbon materials and conductive polymers, which have been mixed with $MnCo_2O_4$ structures,[137,138] such as graphene,[139] CNTs,[140] carbon cloth[116,117] and PPy.[141] Hence, the construction of composites with the combination of two or more different materials has been proved as a promising strategy to boost the electrochemical performance of $MnCo_2O_4$. Due to the electronic conductivity and the specific surface area, rGO has been considered for the formation of composites with $MnCo_2O_4$. Fan *et al.*[142] reported the synthesis of $MnCo_2O_4$/rGO composites with an initial discharge capacity of 1657 mA h g^{-1} at a current density of 0.1 A g^{-1}, and a reversible capacity of 791 mA h g^{-1} at 0.2 A g^{-1} for 100 cycles. A $MnCo_2O_4$@PANi-rGO composite was also synthesized by Huang *et al.*,[143] with a discharge capacity of 745 mA h g^{-1} and a coulombic efficiency of 100% after 1050 cycles at a current density of 500 mA g^{-1}.

3.2.2. Sodium ion batteries. Operating with similar chemistry to Li-ion electrodes, sodium-ion batteries (SIBs) are under intense investigation to overtake LIBs with the advantages of low-cost and safety. Wu and coworkers[144] reported mesoporous Ni-doped $MnCo_2O_4$ hollow nanotubes (MCNO-HNTs) as an anode in SIBs, with a remarkable capacity retention of 81% at 1 A g^{-1} even after 11 000 cycles. Flower-like $MnCo_2O_4$ synthesized by a co-precipitation method exhibited a discharge capacity of 244 mA h g^{-1} after 40 cycles at 50 mA h g^{-1}, which corresponds to 77.1% compared with the second discharge capacity cycle.[145] Table 2 summarizes the performance of different cells of metal ion batteries coupled with different types of electrodes based on $MnCo_2O_4$.

3.2.3. Li–O_2 batteries. Lithium–oxygen batteries have a specific potential energy density of approximately 1700 W h kg^{-1}, which is 5-fold higher than that of conventional current LIBs. This type of device has also significant advantage in their gravimetric energy densities.[149] Transition metal oxides, such as $MnCo_2O_4$, have been investigated as cathodes for Li–O_2 batteries,[150,151] especially due to their low-cost catalyst, good stability, high activity, and simple preparation.[152] Wu *et al.*[153] reported hierarchical porous 3D $MnCo_2O_4$ nanowire bundles as a cathode for Li–O_2 cell application (Fig. 5a), which exhibited specific capacities of 500 and 1000 mA h g^{-1} over 300 and 144 cycles, respectively, and a discharge capacity of 12 919 mA h g^{-1} at 0.1 mA cm^{-2}. More importantly, after two months of cycling, the microstructure of the cathode was maintained and a recyclability of over 200 cycles was achieved. Other structures with high electrochemical performance can be obtained, such as nanotubes[154] (Fig. 5b) and spheres[155,156] (Fig. 5c). Composites are also explored to maximize the electrochemical performance of Li–O_2 batteries, particularly highlighting materials containing porous carbon,[157] Ti_4O_7 [158] and MoO_2/Ni [159].

Large surface areas can provide a promising electrocatalytic activity for the ORR and OER in Li–O_2 batteries. In this way, to enhance the charge transfer rate, composites between $MnCo_2O_4$

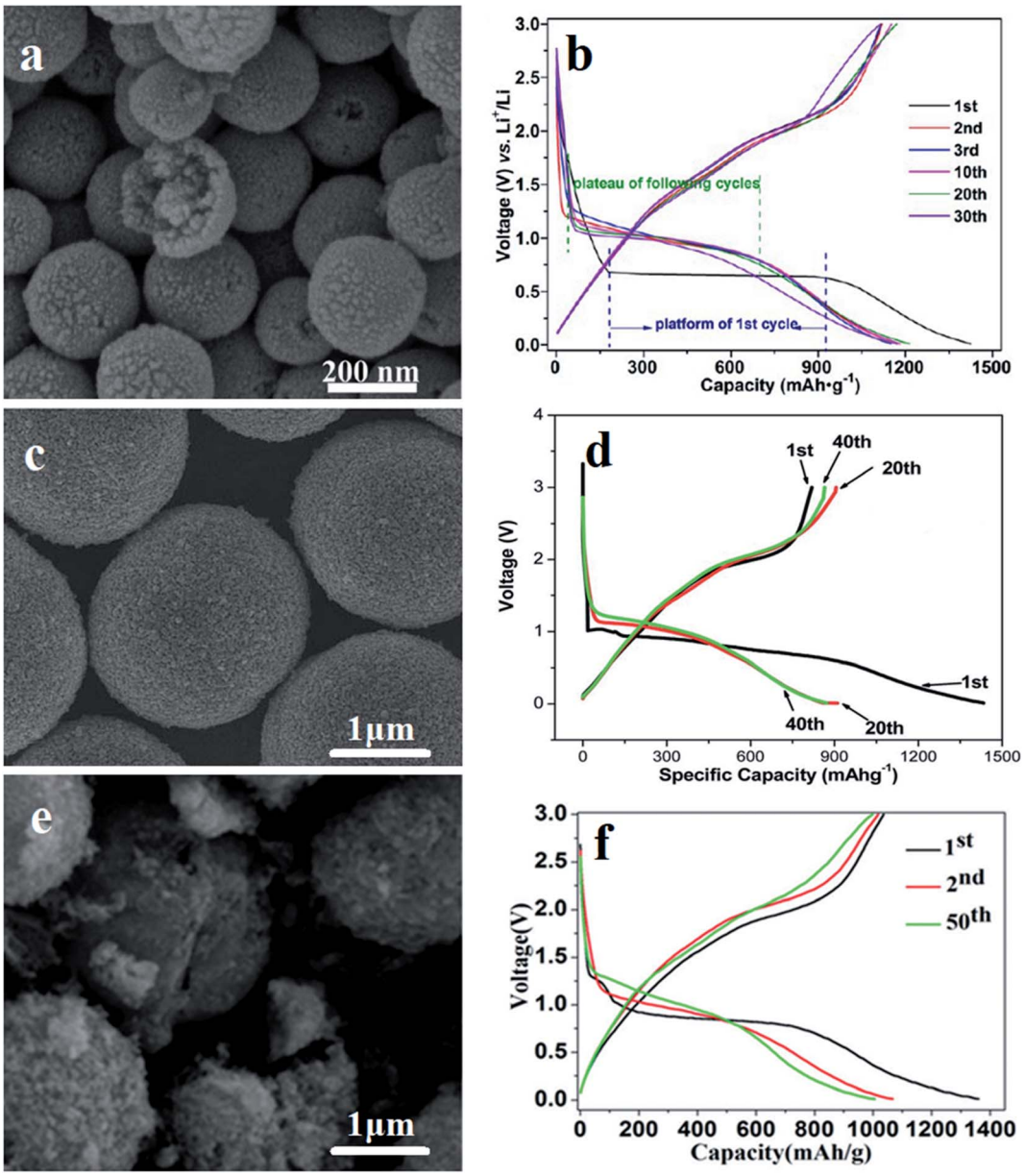

Fig. 4 Scanning electron microscopy images (SEM) and galvanostatic charge–discharge profiles (GCD) of yolk–shell $MnCo_2O_4$. SEM images of (a) hollow $MnCo_2O_4$ submicrospheres. (c) Hierarchical porous $MnCo_2O_4$ yolk–shell microspheres and (e) spherical yolk–shell $MnCo_2O_4$ powders. GCD curves of (b) hollow $MnCo_2O_4$ submicrospheres, (d) hierarchical porous $MnCo_2O_4$ yolk–shell microspheres and (f) spherical yolk–shell $MnCo_2O_4$ powders. (a) and (b) adapted with permission from ref. 120. Copyright © 2014, American Chemical Society. (c and d) adapted with permission from ref. 121. Copyright © Marketplace™, Royal Society of Chemistry. (e and f) adapted with permission from ref. 124. Copyright © Marketplace™, Royal Society of Chemistry.

and carbon materials have been reported.[152,160–163] A peanut shaped $MnCo_2O_4$ which is encapsulated by multi-walled carbon nanotubes (MCO/MWCNTs) was synthesized through a solvothermal method. The batteries exhibited a discharge capacity of 8849 mA h g^{-1} with a restricted voltage of 2 V at 100 mA g^{-1} and a cycle life of 120 times at 100 mA g^{-1} with a limited capacity of 500 mA h g^{-1}.[164]

3.2.4. Other metal–air batteries. $MnCo_2O_4$ electrodes can be prepared as active materials for different metal–air batteries. Ishihara *et al.*[165] studied ORR/OER on mesoporous spinels for Zn–air rechargeable batteries. The $MnCo_2O_4$ spinel showed a surface area of 108 m^2 g^{-1} and an average pore size of 2 nm, providing a decrease of overpotential for the ORR/OER in Zn–air batteries, which showed a stable discharge potential and capacity at 1.05 V and 700 mA h g^{-1}, respectively.

Carbonaceous materials and heteroatom doped-carbon materials were also mixed with $MnCo_2O_4$ due to their intrinsic advantages as ORR catalysts, such as higher surface area and electrochemical stability. Chandrappa *et al.*[166] reported a composite formed by combining $MnCo_2O_4$

Table 2 Performances reported for $MnCo_2O_4$-based metal ion batteries[a]

Battery type	Material type	Material	Initial discharge (mA h g^{-1})	Potential window (V *vs.*)	Reversible capacity (Nth) mA h g^{-1}	Stability (cycle numbers)	Ref.
Lithium ion batteries (LIBs)	Pristine $MnCo_2O_4$	$MnCo_2O_4$ yolk–shell microspheres	1035.8 at 0.1C	0.01–3 Li/Li^+	691.3 (500) at 1C	—	124
		Core–shell ellipsoidal $MnCo_2O_4$	1433.3 at 0.1 A g^{-1}	0.01–3 Li/Li^+	750 (70) at 100 mA g^{-1}	—	128
		Micro-octahedral $MnCo_2O_4$	1438 at 300 mA g^{-1}	0.01–3 Li/Li^+	720.4 (200) at 300 mA g^{-1}	88% (200 cycles)	110
		$MnCo_2O_4$ nanoflakes	1795 at 50 mA g^{-1}	0.01–3 Li/Li^+	925 (50) at 100 mA g^{-1}	—	109
		$MnCo_2O_4$ microspheres	1473 at 60 mA g^{-1}	0.01–3 Li/Li^+	533 (200) at 400 mA g^{-1}	—	106
		$MnCo_2O_4$ cubic microcrystals	1443 at 100 mA g^{-1}	0.01–3 Li/Li^+	—	28% (100 cycles)	104
		$MnCo_2O_4$ needle-shaped	1326 at 60 mA g^{-1}	0.01–3 Li/Li^+	368 (50) at 60 mA g^{-1}	55% (50 cycles)	107
		$MnCo_2O_4$ hollow spheres	1561 at 200 mA g^{-1}	0.01–3 Li/Li^+	1023 (200) at 60 mA g^{-1}	—	122
		$MnCo_2O_4$ hollow submicrospheres	1119 at 400 mA g^{-1}	0.01–3 Li/Li^+	800 (100) at 100 mA g^{-1}	—	120
		$MnCo_2O_4$ quasi-hollow microspheres	1473 at 200 mA g^{-1}	0.01–3 Li/Li^+	610 (100) at 400 mA g^{-1}	—	123
		$MnCo_2O_4$	900 at 60 mA g^{-1}	0.005–3 Li/Li^+	816 (50) 60 mA g^{-1}	—	111
		$MnCo_2O_4$ microspheres	1425.8 at 400 mA g^{-1}	0.005–3 Li/Li^+	1033.3 (200)/400 mA g^{-1}	74.2% (200 cycles)	105
		Dumbbell-shaped porous $MnCo_2O_4$	2073 at 200 mA g^{-1}	0.01–3 Li/Li^+	955(180) at 200 mA g^{-1}	46% (180 cycles)	127
		Erythrocyte like $MnCo_2O_4$	1538 at 200 mA g^{-1}	0.01–3 Li/Li^+	960 (100) at 200 mA g^{-1}	77.6% (100 cycles)	112
		Mesoporous $MnCo_2O_4$ microflowers	1465.1 at 100 mA g^{-1}	0.01–3 Li/Li^+	732 (50) at 100 mA g^{-1}	—	125
		$MnCo_2O_4$ nanospheres	1184.8 at 400 mA g^{-1}	0.01–3 Li/Li^+	749.1 (50) at 200 mA g^{-1}	89.8% (50 cycles)	108
		Porous $MnCo_2O_4$	1750.0 at 400 mA g^{-1}	0.01–3 Li/Li^+	690.1 (100) at 0.5C	—	114
		Flake-like $MnCo_2O_4$	1460 at 100 mA g^{-1}	0.01–3 Li/Li^+	952 (100) at 100 mA g^{-1}	89% (100 cycles)	35
		$MnCo_2O_4$ nanosheets	3.9 mA h cm^{-2} at 800 μA cm^{-2}	0.01–3 Li/Li^+	3.0 mA h cm^{-2} (60) at 800 μA cm^{-2}	—	116
		Porous $MnCo_2O_4$ nanosheets	1044 at 0.2 A g^{-1}	0.01–3 Li/Li^+	848 (200) at 0.2 A g^{-1}	81% (200 cycles)	113
		Porous $MnCo_2O_4$ microspheres	1034 at 1000 mA g^{-1}	0.01–3 Li/Li^+	740 (1000) at 1000 mA g^{-1}	—	115
		Yolk–shell $MnCo_2O_4$ microspheres	1445.1 at 0.2 A g^{-1}	0.01–3 Li/Li^+	860 (40) at 0.2 A g^{-1}	—	121
		$MnCo_2O_4$	1220 at 0.1C	0.1–3 Li/Li^+	907 (50) at 0.5C	90% (50 cycles)	146
		$MnCo_2O_4$ nanotubes	1211.9 at 0.5 A g^{-1}	0.01–3 Li/Li^+	701.4 (320) at 500 mA g^{-1}	—	147
		Porous hydrangea-like $MnCo_2O_4$	1232 at 0.1 A g^{-1}	0.01–3 Li/Li^+	930 (100) at 0.1 A g^{-1}	87% (100 cycles)	126
	$MnCo_2O_4$–metal oxide composite	CoO/$MnCo_2O_{4.5}$ nanorods	1183 at 200 mA g^{-1}	0.01–3 Li/Li^+	1030 (120) at 200 mA g^{-1}	87% (120 cycles)	118
		$MnCo_2O_4$@NC@MnO_2	1380 at 500 mA g^{-1}	0.01–3 Li/Li^+	894 (120) at 500 mA g^{-1}	—	136
		NiO–$MnCo_2O_4$–Ni_6MnO_8	1284 at 30 mA g^{-1}	0.01–3 Li/Li^+	779 (120) at 1C	—	129
		Co_3O_4–$MnCo_2O_4$ powder, 20–50 nm	1781 at 50 mA g^{-1}	0.01–3 Li/Li^+	1250 (200) at 1000 mA g^{-1}	68.2% (200 cycles)	119
		$MnCo_2O_4$–TiO_2 microspheres	1396.9 at 100 mA g^{-1}	0.01–3 Li/Li^+	1271 (200) at 100 mA g^{-1}	91% (200 cycles)	135
		Porous $MnCo_2O_4$@MnO_2	1927.8 at 100 mA g^{-1}	0.0–3 Li/Li^+	1162.8 (200) at 1 A g^{-1}	96% (200 cycles)	134
		NiO–$MnCo_2O_4$ microspheres	1206 at 200 mA g^{-1}	0.01–3 Li/Li^+	846 (50) at 200 mA g^{-1}	—	130
	$MnCo_2O_4$–carbon based composites	3D sandwich-shaped graphene-based $MnCo_2O_4$ hollow spheres	1244 at 200 mA g^{-1}	0.01–3 Li/Li^+	703 (100) at 200 mA g^{-1}	80% (100 cycles)	131
		Graphene-like 2D spinel $MnCo_2O_4$	1157.7 at 0.2 A g^{-1}	0.01–3 Li/Li^+	780 (200) at 0.2 A g^{-1}	—	139
		$MnCo_2O_4$ nanoparticles embedded in graphene sheets	1350 at 100 mA g^{-1}	0.01–3 Li/Li^+	584.3 (250) at 2000 mA g^{-1}	92.3% (250 cycles)	138
		$MnCo_2O_4$@carbon cloth	1886.2 at 1 A g^{-1}	0.01–3 Li/Li^+	1289 (200) at 1 A g^{-1}	—	117
		$MnCo_2O_4$/rGO composite	1657 at 0.1 A g^{-1}	0.01–3 Li/Li^+	791 (100) at 0.2 A g^{-1}	74.1% (100 cycles)	142
		$MnCo_2O_4$/C	1284.5 at 1 A g^{-1}	0.01–3 Li/Li^+	978 (800) at 1 A g^{-1}	—	148
		MWCNT composite	1471 at 946 mA g^{-1}	0.005–3 Li/Li^+	871 (30) at 60 mA g^{-1}	—	140
	$MnCo_2O_4$-conducting polymer composites	$MnCo_2O_4$/polypyrrole	1398 at 200 mA g^{-1}	0.01–3 Li/Li^+	910 (100)/200 mA g^{-1}	—	141
		Flower-like $MnCo_2O_4$@PANi–rGO	—	0.01–3 Li/Li^+	745 (1050)/500 mA g^{-1}	—	143

Table 2 (*Contd.*)

Battery type	Material type	Material	Initial discharge (mA h g^{-1})	Potential window (V *vs.*)	Reversible capacity (Nth) mA h g^{-1}	Stability (cycle numbers)	Ref.
	Other $MnCo_2O_4$-based composite materials	$Mn_{0.4}Ni_{0.6}Co_2O_4$ nanowires	1054 at 0.1 A g^{-1}	0.01–3 Li/Li^+	706 (200) at 500 mA g^{-1}	98% (200 cycles)	132
		$MnCo_2O_4$ porous nanospheres@N-doped carbon	1099.9 at 1 A g^{-1}	0.01–3 Li/Li^+	883.3 (500) at 1 A g^{-1}	—	137
		Ni-doped $MnCo_2O_4$ submicron-spheres	1849 at 0.2 A g^{-1}	0.01–3 Li/Li^+	174.7 (2000) at 5 A g^{-1}	—	133
Sodium ion batteries	—	Mesoporous Ni-doped $MnCo_2O_4$ hollow nanotubes	340 at 0.1 A g^{-1}	0.01–3 Na/Na^+	109 (11 000) at 1 A g^{-1}	81% (11 000 cycles)	144
	—	Flower-like $MnCo_2O_4$	697 at 25 mA g^{-1}	0.01–3 Na/Na^+	244 (40) at 50 A g^{-1}	77.1% (40 cycles)	145
	$MnCo_2O_4$-carbon based composites	$MnCo_2O_4$/nanographene	1120 at 0.05 A g^{-1}	0.01–3 Na/Na^+	541.2 (200) at 0.05 A g^{-1}	—	77

[a] rGO = reduced graphene oxide, MWCNT = multi wall carbon nanotube, PANi = polyaniline, and NC = N-doped carbon.

nanospheres with graphene sheets (MCO/GS) as a bifunctional cathode catalyst for Zn–air batteries. The electrochemical measurements revealed a unique small charge–discharge overpotential, cycling stability and higher rate capability than a bare MCO catalyst. Carbon coated $MnCo_2O_4$ nanowires ($MnCo_2O_4$@C) were also used as a bifunctional oxygen catalyst for rechargeable Zn–air batteries. The authors recorded an excellent electrochemical performance and improved cycling stability, with an onset potential of 0.92 V and current retention rate of 99% within 10 000 s at 0.80 V *vs.* RHE.[167] Besides Zn–air batteries,[166–169] Na–air devices have also been reported in the literature.[170,171] Table 3 summarizes the performance of different cells coupled with different metal–air batteries of electrodes based on $MnCo_2O_4$.

4. $MnCo_2O_4$-based electrocatalysts for energy conversion and storage

4.1. ORR catalysts in energy storage

As already highlighted in the previous topics, the development of high-performance electrocatalysts is essential for achieving high-performance energy devices, especially catalysts for oxygen reactions (OER and ORR) due to the sluggish reaction kinetics, which often requires a large overpotential to sustain a reasonable rate of electrode reactions.[172] In fact, the design and optimization of catalysts for the ORR/OER is of fundamental importance for the development of more efficient and competitive energy storage devices, such as for metal–air batteries[173] and proton exchange membrane fuel cells (PEMFCs).[174]

Currently, Ir and/or Ru based oxides and Pt-based materials are the most widely used catalysts for the OER and ORR, respectively. However, the high cost, scarcity, and poor bifunctional activity of precious metals greatly hinder their industrial application on a large scale.[175] To solve these disadvantages, intensive efforts have been devoted to development of noble metal-free oxygen reaction catalysts with low cost and high activity in the past decades,[176] especially for ORR catalysts. Among these reported noble metal-free ORR catalysts or bifunctional oxygen electrocatalysts, $MnCo_2O_4$ and $MnCo_2O_4$-derived composites show great potential as electrocatalysts because of their high intrinsic activity, and the corresponding activities can be further tuned through their phase and composition.[177]

In fact, based on Table 4, it is possible to perceive important and well-known strategies that have been employed in the design of electrocatalysts containing $MnCo_2O_4$ for the ORR, as for example: (1) active site engineering, obtained through the control of size, morphology and defects, as well as the crystalline phase, in order to maximize the density of active sites,[3,178] and (2) conductivity optimization, obtained especially by doping with hetero-atoms and/or by formation of composites with conducting materials.[3,178,179]

As an excellent example of the active site engineering strategy, Yang *et al.*[180] successfully reported a facile precursor pyrolysis method to prepare porous spinel cobalt manganese oxides with tunable size, shape, chemical composition and

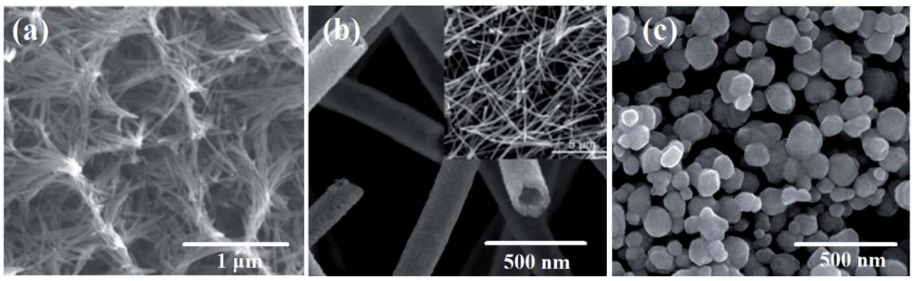

Fig. 5 Scanning electron microscopy images (SEM) of different morphologies of $MnCo_2O_4$. SEM images of (a) $MnCo_2O_4$ nanowires, (b) single-wall $MnCo_2O_4$ nanotubes and (c) $MnCo_2O_4$ nanospheres. Fig. 1a adapted with permission from ref. 53. Copyright © 2017, American Chemical Society. Fig. 1b, adapted with permission from ref. 154. Copyright © Marketplace™, Royal Society of Chemistry. Fig. 1c adapted with permission from ref. 155. Copyright © Marketplace™, Royal Society of Chemistry.

crystalline structure *via* a facile precursor pyrolysis method (Fig. 6a). The capping agent and reaction temperature in the reaction were found to be crucial in the formation of porous spinel cobalt manganese oxides from cubic Co_2MnO_4 nanorods (c-CMO NRs) to tetragonal $CoMn_2O_4$ microspheres (t-CMO MSs) and tetragonal $CoMn_2O_4$ cubes (t-CMO CBs).

Table 3 Performances reported for $MnCo_2O_4$-based metal–air batteries

Type	Cathodes	Initial discharge (mA h g^{-1})	Discharge voltage (V)	Charge voltage (V)	Overpotential[a] (V)	Stability (cycle numbers)	Ref.
Na air battery	Co_3O_4@$MnCo_2O_{4.5}$ nanocubes	8400 at 500 mA g^{-1}	2.3	2.75	0.45	(135 cycles)	171
	dp-$MnCo_2O_4$/N-rGO	—	2.75	3.14	0.39	(25 cycles)	170
	Ni-doped hollow nanotubes	340.5 at 0.1 A g^{-1}	—	—	—	81% (11 000 cycles)	144
Zn air battery	$MnCo_2O_4$ nanofibers	125 at 10 mA cm^{-2}	—	—	1.23	(500 cycles)	168
	$MnCo_2O_4$ nanoparticles embedded in nitrogen-doped macroporous carbon nanofiber arrays	—	—	—	0.55	(100 cycles)	169
	$MnCo_2O_4$@C nanowires	—	—	—	0.89	—	167
Li air battery	$MnCo_2O_4$@Ni	10 520 at 100 mA g^{-1}	2.79	—	0.65	1000 mA h g^{-1} (119 cycles)	150
	Nanowires	12 919 at 0.1 mA cm^{-2}	2.92	3.46	0.54	1000 mA h g^{-1} (144 cycles)	153
	Microspheres	2809.1 at 500 mA g^{-1}	2.7	3.9	—	1000 mA h g^{-1} (50 cycles)	156
	P-Doped hierarchical porous carbon	13 150 at 200 mA g^{-1}	2.75	4.0	—	1000 mA h g^{-1} (200 cycles)	157
	Ti_4O_7/$MnCo_2O_4$	5400 at 100 mA g^{-1}	2.85	3.6	0.75	500 mA h g^{-1} (100 cycles)	158
	$MnCo_2O_4$ nanospheres	8518 at 100 mA g^{-1}	2.86	—	0.85	1000 mA h g^{-1} (20 cycles)	155
	$MnCo_2O_4$ nanorods	1334 at 0.1 mA cm^{-2}	2.61	4.10	—	500 mA h g^{-1} (40 cycles)	151
	$MnCo_2O_4$/graphene	3784 at 100 mA g^{-1}	2.95	3.75	~0.8	1000 mA h g^{-1} (40 cycles)	162
	Peanut shaped $MnCo_2O_4$/MWCNTs	8849 at 100 mA g^{-1}	—	—	—	500 mA h g^{-1} (120 cycles)	164
	$MnCo_2O_4$/graphene	10 092 at 100 mA g^{-1}	2.9	3.7	0.8	1000 mA h g^{-1} (250 cycles)	161
	$MnCo_2O_4$@carbon cloth	7238 at 200 mA g^{-1}	—	—	1.46	500 mA h g^{-1} (108 cycles)	160
	$MnCo_2O_4$–graphene	11 092.1 at 200 mA g^{-1}	—	—	—	1000 mA h g^{-1} (35 cycles)	163
	Double-wall $MnCo_2O_4$ nanotubes	8100 at 100 mA g^{-1}	2.77	4.14	1.37	1000 mA h g^{-1} (278 cycles)	154
	$MnCo_2O_4$/MoO_2@Ni nanosheets	4210 at 200 mA g^{-1}	—	—	0.75	(400 cycles)	159
	$MnCo_2O_4$ nanowires	8364 at 200 mA g^{-1}	—	—	0.823	500 mA h g^{-1} (167 cycles)	152

[a] The overpotential was calculated based on the difference of discharge–charge voltage plateaus. rGO = reduced graphene oxide, MWCNT = multi wall carbon nanotube, and C = carbon.

Table 4 Catalytic activity parameters of recently reported ORR $MnCo_2O_4$-based electrocatalysts[a]

ORR catalysts	Incorporated or doping atom	Substrate	E_{ORR} onset potential (V *vs.* RHE)	Half wave potential (V *vs.* RHE)	E_{ORR} at −3 mA cm^{-1} (V *vs.* RHE)	E_{OER} at 10 mA cm^{-1} (V *vs.* RHE)	ΔE E_{OER}–E_{ORR} (V *vs.* RHE)	Current density (mA cm^{-1})	Tafel slope (mV dec^{-1})	Average electron transfer number (n)	Stability (h)	pH condition	Ref.
MCO-700	—	GCE	—	—	—	—	—	6.69 mA cm^{-1}	—	3.2–3.5	−16.66	0.1 M KOH	189
CMO-3.9/CNT	CNT	GCE	—	0.86	—	1.61	—	2.90 mA cm^{-1} at 0.7 V	65–126	3.98	94% 8.33	0.1 M KOH	190
$MnCo_2O_4$	—	—	0.88	0.77	—	—	—	—	—	—	87% 5.55	0.1 M KOH	167
$MnCo_2O_4$@C	Carbon	—	0.92	0.80	—	1.66	0.89[d]	—	—	3.61	99% 5.55	0.1 M KOH	167
$MnCo_2O_4$/C	Vulcan carbon	GCE	—	0.76	—	~1.74	—	—	~61	3.51	−8.33	0.1 M KOH	184
$MnCo_2O_4$/C nanosheets	Porous C nanosheets	GCE	0.945	0.767	—	—	—	—	—	3.82	72.5% 2.77	0.1 M KOH	183
$MnCo_2O_4$	—	GCE	~0.83[a], 1.12	0.66	—	—	—	−2.30 mA cm^{-1} at 0.36 V	−142.2	—	−2.22	0.1 M KOH	20
$MnCo_2O_4$-rGO	rGO	GCE	~0.89[a], 1.11	0.77	—	—	—	−3.33 mA cm^{-1} at 0.36 V	−150.1	3.8	−2.22	0.1 M KOH	20
MCO	—	GCE	−0.165	−0.225	−0.647	0.840	1.487	—	145	$n > 3$	—	0.1 M KOH	21
MCO + NS-MCS	NS-MCS	GCE	−0.112	−0.186	−0.221	0.817	1.038	−4.60 mA cm^{-1} at −1.0 V	131	$n > 3$	—	0.1 M KOH	21
MCO/NS-MCS	NS-MCS	GCE	−0.079	−0.160	−0.186	0.774	0.960	−5.03 mA cm^{-1} at −1.0 V	124	3.64–3.88	82.3% 5.55	0.1 M KOH	21
$MnCo_2O_4$ at 500 °C	—	GCE	0.81[a]	0.58	—	—	—	—	—	—		0.1 M KOH	22
N-MWCNT-$MnCo_2O_4$ at 500 °C	N-MWCNT	GCE	0.83[a], 0.86	0.75	—	—	—	—	—	3.9	−20	0.1 M KOH	22
N-MWCNT-$MnCo_2O_4$ at 500 °C	N-MWCNT	GCE	0.86[a]	0.60	—	—	—	—	—	—	—	0.1 M KOH	22
MCO	—	GCE	—	—	<0.1	>1.9	>2	—	—	—	—	0.1 M KOH	177
MCO + NCNTs	NCNTs	GCE	—	—	0.70	1.74	1.04	—	—	—	—	0.1 M KOH	177
MCO@NCNTs	NCNTs	GCE	—	—	0.76	1.70	0.94	—	−96 and −125	3.9	—	0.1 M KOH	177
$MnCo_2O_4$/CNT	CNT	GCE	—	—	—	—	—	—	—	3.75	—	0.1 M KOH	191
$MnCo_2O_4$/N,S-CNT	N,S-CNT	GCE	—	—	—	—	—	—	—	3.83	72%, 5	0.1 M KOH	191
$MnCo_2O_4$/rGO	rGO	GCE	0.94	0.78	—	—	—	—	75.4	3.90	—	0.1 M KOH	185
$MnCo_2O_4$/3D-G	3D-G	GCE	0.98	0.81	—	—	—	—	68.5	3.96	79.84%, 60	0.1 M KOH	185

Table 4 (*Contd.*)

ORR catalysts	Incorporated or doping atom	Substrate	E_{ORR} onset potential (V *vs.* RHE)	Half wave potential (V *vs.* RHE)	E_{ORR} at −3 mA cm^{-1} (V *vs.* RHE)	E_{OER} at 10 mA cm^{-1} (V *vs.* RHE)	ΔE E_{OER}–E_{ORR} (V *vs.* RHE)	Current density (mA cm^{-1})	Tafel slope (mV dec^{-1})	Average electron transfer number (n)	Stability (h)	pH condition	Ref.
$MnCo_2O_4$/CNTs	CNTs	GCE	0.93	0.74	—	—	—	—	84.6	3.81	—	0.1 M KOH	185
$MnCo_2O_4$/C	C	GCE	0.92	0.72	—	—	—	—	87.4	3.76	—	0.1 M KOH	185
$MnCo_2O_4$	—	—	0.865	0.552	—	—	—	−3.26 mA cm^{-1} at 0.2 V	—	—	—	0.1 M KOH	186
$MnCo_2O_4$ + N–C	N–C	—	0.918	0.780	—	—	—	−5.28 mA cm^{-1} at 0.2 V	—	—		0.1 M KOH	186
$MnCo_2O_4$/N–C	N–C	—	0.943	0.795	—	—	—	−5.78 mA cm^{-1} at 0.2 V	86	3.50–3.83	89.68% 2.77	0.1 M KOH	186
CoMn/pNGr (2 : 1)	pNGr	GCE	0.94[a], 0.9[a]	0.791	—	—	—	—	74	3.98	−5000 cycles	0.1 M KOH	192
CoMn/pNGr (1 : 1)	pNGr	GCE	0.9[a]	0.726	—	—	—	—	—	3.66	—	0.1 M KOH	192
CoMn/pNGr (1 : 2)	pNGr	GCE	0.92[a]	0.734	—	—	—	—	—	3.46	—, —	0.1 M KOH	192
$MnCo_2O_4$/NGr	NGr	GCE	0.86[a]	0.648	—	—	—	—	—	—	—, —	0.1 M KOH	192
$MnCo_2O_4$/N-rmGO	N-rmGO	GCE	0.95[a, c]	—	—	—	—	—	36[c]	∼3.9[c]	96.5% 5.55	1 M KOH	188
$MnCo_2O_4$ + N-rmGO	N-rmGO mixture	GCE	0.91[a, c]	—	—	—	—	—	—	∼3.7[c]	∼75% 5.55	1 M KOH	188
Mesoporous $MnCo_2O_4$	—	GCE	0.95[a]	—	0.80	1.63	0.83	—	—	3.94	85% 10	0.1 M KOH	182
m-$MnCo_2O_4$	—	GCE	−0.04	—	—	—	—	—	−95	3.96	87% 95	0.1 M KOH	181
$MnCo_2O_4$/C	C	GCE	0.93[c]	0.76[c]	—	1.52[c]	0.59[c]	—	68/207[c]	3.92[c]	−24	1 M KOH	193
dp-$MnCo_2O_4$/CNT	CNT	GCE	−0.11[b]	—	—	—	—	−5.33 mA cm^{-1} at −0.8 V[b]	106	∼4.0	—, —	0.1 M KOH	194
dp-$MnCo_2O_4$/N-rGO	N-rGO	GCE	−0.09[b]	—	—	—	—	−5.71 mA cm^{-1} at −0.8 V[b]	65	∼4.0	—, —	0.1 M KOH	194
$MnCo_2O_4$	—	GCE	0.84	0.59	0.55	1.77	1.22	—	78.8	2.5–3.7	—	0.1 M KOH	187
CMO/20N-rGO	N-rGO	GCE	0.93	0.79	0.77	1.68	0.91	—	50.8	3.9–4	86.3% 8	0.1 M KOH	187
NCNTs	NCNTs	GCE	—	—	—		—	—	—	3.4	—, —	0.1 M KOH	195
NCNT-500	NCNTs	GCE	—	—	—	1.495	—	—	—	3.8	—, —	0.1 M KOH	195
$MnCo_2O_3$/C	C	GCE	—	0.86[c]	—	—	—	—	45[c]	—	—, 10 000 cycles	1 M KOH	196

Table 4 (*Contd.*)

ORR catalysts	Incorporated or doping atom	Substrate	E_{ORR} onset potential (V *vs.* RHE)	Half wave potential (V *vs.* RHE)	E_{ORR} at −3 mA cm^{-1} (V *vs.* RHE)	E_{OER} at 10 mA cm^{-1} (V *vs.* RHE)	ΔE E_{OER}–E_{ORR} (V *vs.* RHE)	Current density (mA cm^{-1})	Tafel slope (mV dec^{-1})	Average electron transfer number (n)	Stability (h)	pH condition	Ref.
$MnCo_2O_4$/C	C	GCE	—	0.84[c]	—	—	—	—	50[c]	—	—, 10 000 cycles	1 M KOH	196
c-CMO NRs	—	GCE	0.9	0.72	—	—	—	5.9 mA cm^{-1}	—	3.9	95%, 2.77	0.1 M KOH	180
t-CMO MSs	—	GCE	0.89	0.70	—	—	—	5.5 mA cm^{-1}	—	∼3.8	95%, 2.77	0.1 M KOH	180
t-CMO CBs	—	GCE	0.89	0.65	—	—	—	5.51 mA cm^{-1}	—	3.6	89%, 2.77	0.1 M KOH	180
$MnCo_2O_3$/CNF	CNF	GCE	−0.08[b]	−0.21[b]	—	—	1.04	—	—	∼3.96	89%, 8.33	0.1 M KOH	197
D-AC@2Mn–4Co	D-AC	GCE	883	803	—	—	—	4.72 mA cm^{-1} at 0.2 V	37.5	3.83	92.7%, 20 000	0.1 M KOH	198
Co_2MnO_4	—	—	—	—	0.59	1.92	1.33	—	3.89	—	—, —	0.1 M KOH	199
Co_3O_4 + Co_2MnO_4	—	—	—	—	0.55	1.86	1.31	—	3.85	—	—, —	0.1 M KOH	199
Co_3O_4/Co_2MnO_4	—	—	—	—	0.68	1.77	1.09	—	3.97	—	∼94%, 2.77	0.1 M KOH	199

[a] a = obtained by cyclic voltammetry, b = *vs.* Ag/AgCl, — = information not found in the paper, c = 1 M KOH, d = $\Delta E = |E_{j10}| - |E_{1/2}|$, MCO/NS-MCS = cobalt spinel oxides supported on nitrogen and sulfur co-doped mesoporous carbon spheres, N-doped MWCNT = nitrogen-doped multi-walled carbon nanotube, N,S-CNT = N,S-doped carbon nanotubes, 3D-G = three-dimensional graphene, N–C = N-doped carbon, pNGr = N-doped porous graphene, D-AC = AC-based defective carbon, t-CMO CBs = tetragonal $CoMn_2O_4$ cubes, tetragonal $CoMn_2O_4$ microspheres, and c-CMO NRs = cubic Co_2MnO_4 nanorods.

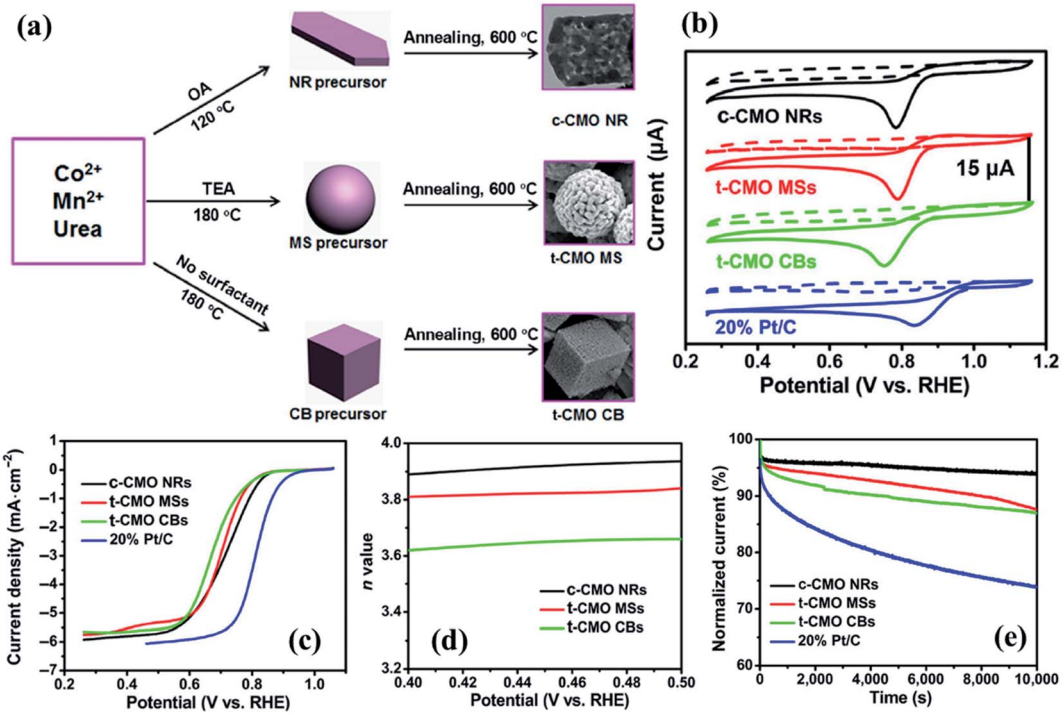

Fig. 6 (a) The synthetic process of different spinel $Co_xMn_{3-x}O_4$. ORR data of the prepared CMOs in O_2 *versus* Ar-saturated 0.1 M KOH with a catalyst mass loading of 0.21 mg cm^{-2}. (b) Cyclic voltammetry curves of electrocatalysts in O_2 *versus* Ar-saturated 0.1 M KOH. (c) Linear sweep voltammograms of the electrocatalysts in 0.1 M KOH at 1600 rpm. (d) Electron transfer number *n* at different potentials. (e) Chronoamperometric responses (percentage of current retained *versus* operation time) of the different spinel CMOs and 20% Pt/C kept at 0.50 V *vs.* RHE in O_2-saturated 0.1 M KOH. Reproduced with permission from ref. 180. Copyright © 2016, Tsinghua University Press and Springer-Verlag Berlin Heidelberg.

As illustrated in CVs (Fig. 6b) and polarization curves (Fig. 6c) of porous CMOs and 20% Pt/C, all the prepared spinel CMOs exhibited good ORR electrocatalytic activities, of which the c-CMO NRs showed a much more positive onset potential of 0.9 V and a half-wave potential of 0.72 V, which are very close values to those obtained by a commercial Pt/C. Furthermore, the *n* value of the c-CMO NRs in ORR electrocatalysis was calculated to be about 3.9 in the range of 0.45 and 0.60 V (Fig. 6d, which is in good agreement with a 4-electron oxygen reduction process) and demonstrated a desired durability with negligible degradation of their electrocatalytic activity after a continuous operation time of 10 000 seconds (Fig. 6e), which is much better than that of the commercial Pt/C electrocatalyst.[180]

The active site engineering strategy has also been used in the development of a mesoporous $MnCo_2O_4$ electrode material.[181] In one of these studies, Wang and co-workers[182] reported a mesoporous bifunctional oxygen $MnCo_2O_4$ electrocatalyst synthesized through a spray-pyrolysis route (Fig. 7a), with Mn^{IV} in the surface and Mn^{III} in the bulk while Co^{II} was present both in the surface and bulk, as confirmed by X-ray near-edge structure (XANES) and XPS investigation. As a result, the $MnCo_2O_4$ exhibited both Co_3O_4-like activity for the OER (Fig. 7b) and Mn_2O_3-like performance for the ORR (Fig. 7c), with a potential difference between the ORR and OER of 0.83 V. According to the Koutecky–Levich (K–L) equation, the electron transfer number (*n*) of $MnCo_2O_4$ was calculated to be 3.94 and after 10 h, the loss of current density for $MnCo_2O_4$ was only 15%, indicating higher stability of $MnCo_2O_4$ than Pt/C (Fig. 7e). Another advantage is that the electrode material can be obtained on a large-scale at a relatively low temperature with precise chemical control of the components. The prominent bifunctional activity shows that $MnCo_2O_4$ could be used in metal–air batteries and/or other energy devices, as confirmed by the home-build Zn–air battery used to study the bifunctional stability of mesoporous $MnCo_2O_4$ (Fig. 7e).[182]

On the other hand, conductivity optimization by the formation of composites with conducting carbon materials has been the main strategy for preparing excellent electrocatalysts for the ORR. In fact, pure $MnCo_2O_4$ nanoparticles displayed certain ORR catalytic activity, but with a poor onset potential and peak potential.[183] In this context, among the most used carbon materials for this application, it is possible to highlight Vulcan carbons,[184] CNTs[22] and graphene derivatives.[20]

In one of these studies, Zhang *et al.*[185] designed a strategy to prepare $MnCo_2O_4$ on three-dimensional graphene (3D-G), as shown in Fig. 8. Typically, 3D-G (with multilayered structure of graphene) was synthesized using a coal tar pitch as the carbon source and nano MgO as the template (Fig. 8a). Then, spinel $MnCo_2O_4$ nanoparticles were *in situ* prepared and deposited on the inner walls of pores in the 3D-G by a facile hydrothermal method, resulting in the $MnCo_2O_4$/3D-G composite.[185]

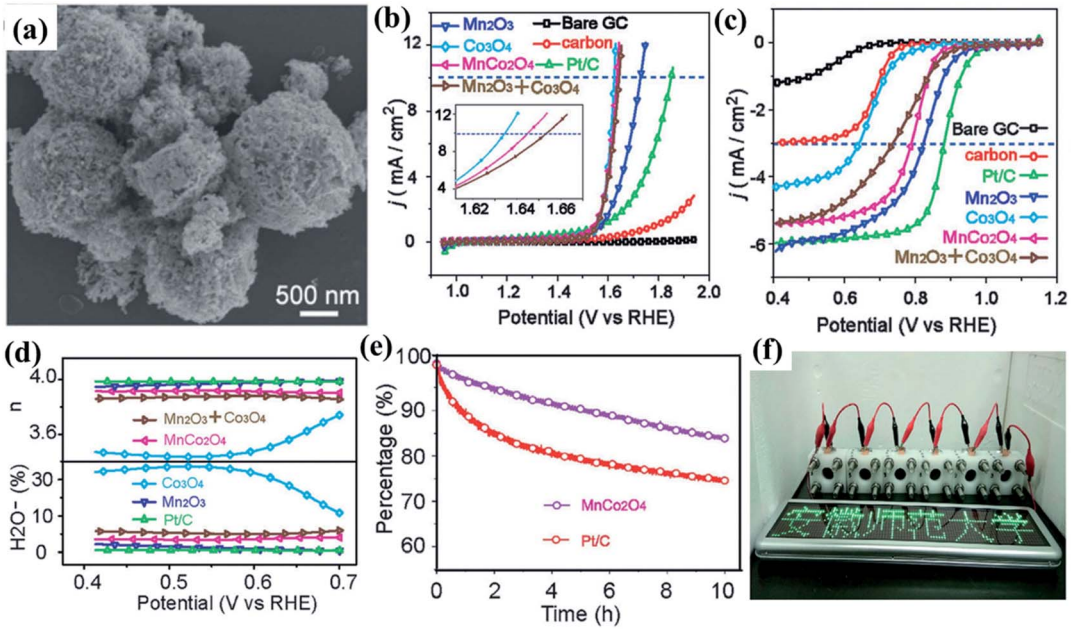

Fig. 7 (a) SEM of $MnCo_2O_4$; (b) OER polarization curves of catalysts at 1600 rpm; (c) ORR polarization curves of catalysts at 1600 rpm; (d) percentage of peroxide and electron numbers (*n*) of Co_3O_4, Mn_2O_3, $MnCo_2O_4$, Pt/C, and the physical mixture of Mn_2O_3 and Co_3O_4. (e) Chronoamperometric measurements of $MnCo_2O_4$ and Pt/C at −0.3 V (V *vs.* Ag/AgCl) in O_2-saturated 0.1 M KOH at 1600 rpm. (f) A green light emitting diode (LED) panel powered by six Zn–air batteries (containing $MnCo_2O_4$). Reproduced with permission from ref. 182. Copyright © 2017 Wiley-VCH Verlag GmbH & Co. KGaA, Weinheim University Press and Springer-Verlag Berlin Heidelberg.

Surprisingly, the $MnCo_2O_4$/3D-G catalyst showed an onset potential of 0.98 V (*vs.* RHE) and the half-wave potential was 0.81 V (*vs.* RHE) in a solution of 0.1 M KOH (Fig. 8b), which was clearly superior to those of 20 wt% Pt/C (0.97 V, 0.80 V), $MnCo_2O_4$/rGO (0.94 V, 0.78 V), $MnCo_2O_4$/CNTs (0.93 V, 0.74 V), and $MnCo_2O_4$/C (0.92 V, 0.72 V).[185] In addition, the electron transfer number was 3.96 at 0.4 V (*vs.* RHE), and its catalyzed ORR mainly follows a four-electron process (Fig. 8c), indicating that the $MnCo_2O_4$/3D-G catalyst possesses superior selectivity for the ORR process. Besides that, $MnCo_2O_4$/3D-G showed the lowest Tafel slope of 68.5 mV dec^{-1} compared to those of Pt/C (70.2 mV dec^{-1} of 20 wt%), $MnCo_2O_4$/rGO (75.4 mV dec^{-1}), $MnCo_2O_4$/CNTs (84.6 mV dec^{-1}) and $MnCo_2O_4$/C (87.4 mV dec^{-1}) (Fig. 8d), and the durability test demonstrated that the

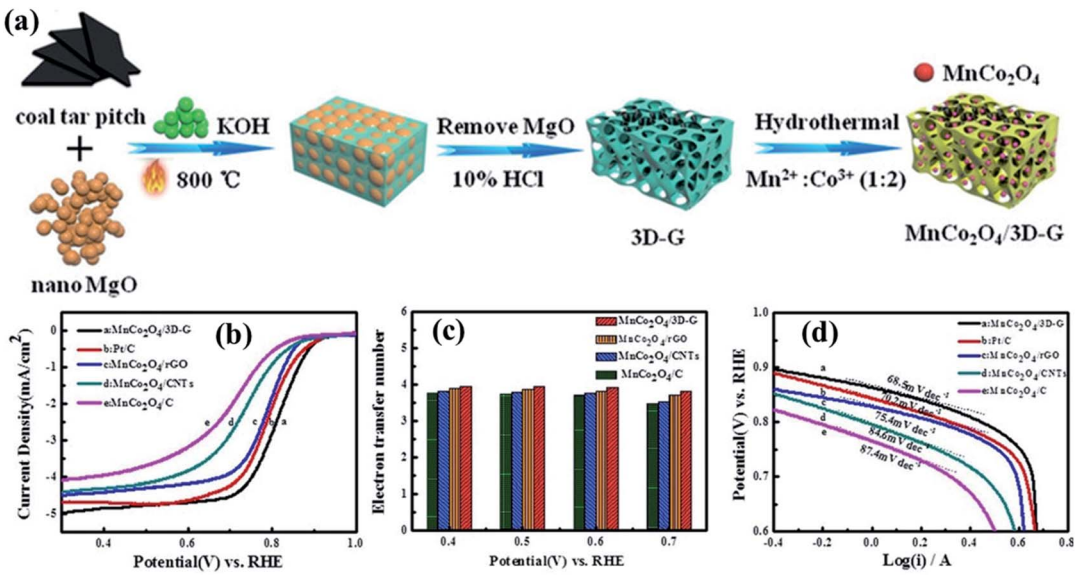

Fig. 8 (a) The synthesis route to the $MnCo_2O_4$/3D-G catalyst. (b) LSV curves of the different catalysts. (c) Electron transfer number per oxygen molecule of the different catalysts at different potentials. (d) Tafel slopes of the electrode assemblies fabricated with different catalysts. Reproduced with permission from ref. 185. Copyright © 2018 Wiley-VCH Verlag GmbH & Co. KGaA, Weinheim.

$MnCo_2O_4$/3D-G catalyst has a much better durability than commercial Pt/C.[185] This work shows that the preparation of composites with carbonaceous materials is really an inspiring strategy to prepare high performance electrocatalysts for the development of fuel cells.

It is important to highlight that results as promising as those obtained in the work by Zhang *et al.*[185] were obtained by forming composites (conductivity optimization strategy) with conductive carbonaceous materials, applying the active site engineering strategy to the catalytic nanocarbon sites of these composites. In this combination of strategies, N and S-doped carbonaceous materials have been intensively studied,[21] for example, Fu and co-workers[186] successfully prepared composed of N-doped carbon (N–C) and $MnCo_2O_4$ NPs for the ORR ($MnCo_2O_4$/N–C), with an ORR onset potential of 0.943 V, ORR half-wave potential of 0.795 V, synthesized by pyrolyzing the mesoporous-silica-protected zeolitic imidazolate framework-8 (ZIF-8) and etching, followed by a facile hydrothermal procedure (Fig. 9a). The superior performance of $MnCo_2O_4$/N–C was attributed to its porous structure and large surface area, N-doping effect, small size $MnCo_2O_4$ NPs and synergistic effects between the doped active species.[186] Based on the values of onset and half-wave potentials shown in Table 1, it is possible to infer that the $MnCo_2O_4$/N–C reported by Fu *et al.*[186] presented slightly better performance than other composites containing N-doped carbonaceous materials, such as N-MWCNT-$MnCo_2O_4$ (ORR onset potential of 0.86 V, ORR half-wave potential of 0.75 V),[22] and CMO/20N-rGO (ORR onset potential of 0.93 V, ORR half-wave potential of 0.79 V).[187]

Using a slightly different approach, Liang *et al.*[188] developed hybrid composites through direct NP nucleation and growth on nitrogen doped-reduced graphene oxide (N-rmGO) sheets and Mn substitution of spinel Co_3O_4 NPs (average size of ~5 nm) for the ORR under alkaline conditions (Fig. 9b), as confirmed by the SEM (Fig. 9c) and TEM (Fig. 9d) images, as well as by the HRTEM images, showing the lattice fringes of the nanocrystals, consistent with the $MnCo_2O_4$ crystal structure (Fig. 9e). This method results in covalent coupling between oxide NPs and N-

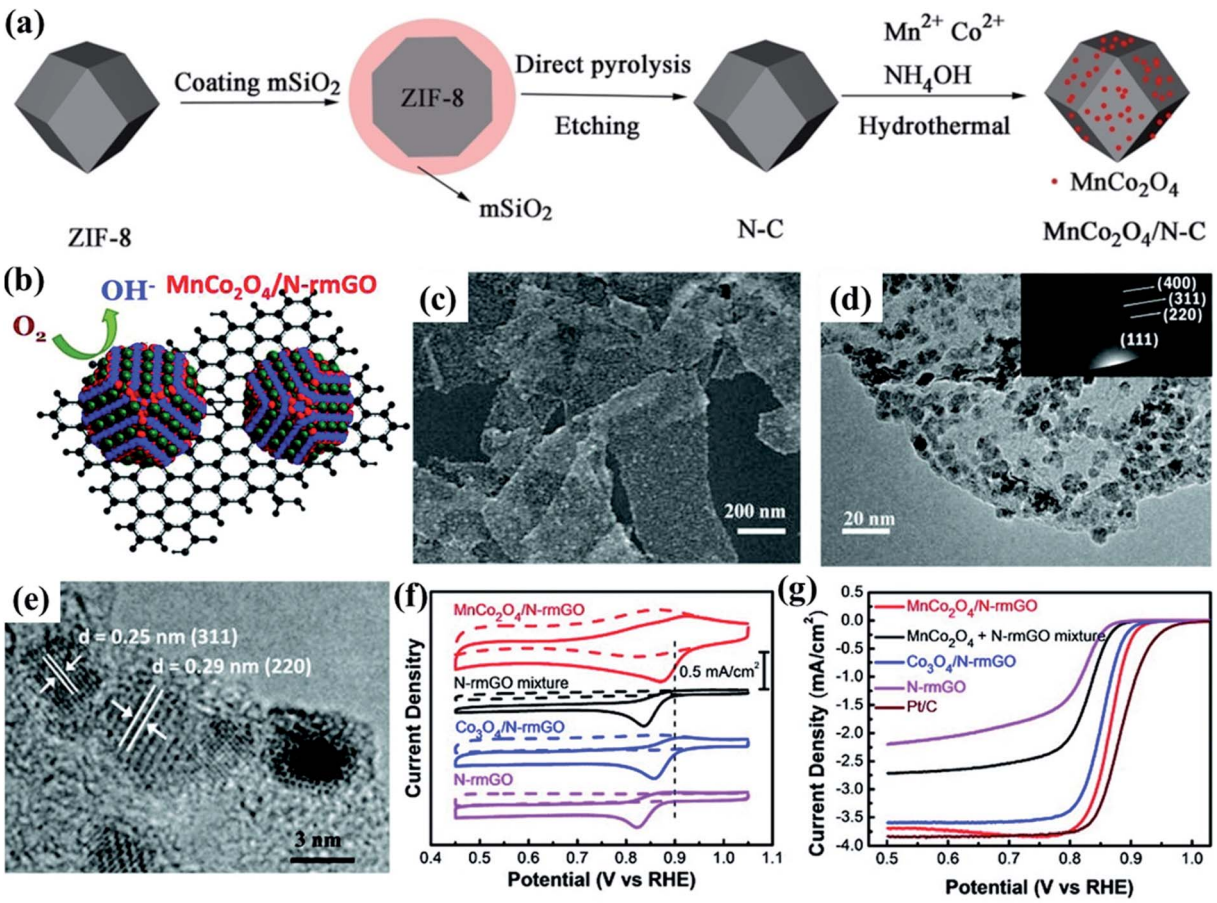

Fig. 9 Schematic illustration of preparation of (a) $MnCo_2O_4$/N–C nanocomposites. Reproduced with permission from ref. 186. Copyright © 2018 Wiley-VCH Verlag GmbH & Co. KGaA, Weinheim. Schematic illustration of preparation of (b) the $MnCo_2O_4$/N-rmGO hybrid. (c) SEM image and (d) TEM image with an inset of the electron diffraction pattern of the $MnCo_2O_4$/N-rmGO hybrid, respectively. (e) A high-magnification TEM image of the $MnCo_2O_4$/N-rmGO hybrid. (f) CV curves of the $MnCo_2O_4$/N-rmGO hybrid, $MnCo_2O_4$ + N-rmGO mixture, Co_3O_4/N-rmGO hybrid, and N-rmGO on glassy carbon electrodes in O_2-saturated (solid line) or N_2-saturated (dashed line) 1 M KOH. The peak position of Pt/C was shown as a dashed line for comparison. (g) Rotating-disk electrode voltammograms of the $MnCo_2O_4$/N-rmGO hybrid, $MnCo_2O_4$ + N-rmGO mixture, Co_3O_4/N-rmGO hybrid, N-rmGO, and Pt/C in O_2-saturated 1 M KOH at a sweep rate of 5 mV s^{-1} at 1600 rpm. Reproduced with permission from ref. 188. Copyright © 2018 Wiley-VCH Verlag GmbH & Co. KGaA, Weinheim.

rmGO sheets, yielding higher activity and stronger durability than the physical mixture of NPs and N-rmGO.[188]

Interestingly, the C–O and C–N bonds in the N-rmGO sheet were strongly perturbed, suggesting the formation of C–O–metal and C–N–metal bonds between N-rmGO and spinel oxide NPs, as confirmed by electrochemical and XANES investigations. As a result, the composite showed a more positive onset (0.95 V *vs.* RHE, Fig. 9f–g) and a greater electron transfer number (~3.9) than the corresponding physical mixture of $MnCo_2O_4$ NPs and N-rmGO (0.91 V *vs.* RHE and the electron transfer number = ~3.7).[188] Based on the above, it is feasible to mention that the combination of conductivity optimization and active site engineering strategies should benefit the design of advanced ORR electrocatalysts for energy conversion and storage.

4.2. Water-splitting electrocatalysts for energy conversion (OER and HER)

Over the years, the energy demand has increased significantly, and this consumption has intensified year after year, which has led to the depletion of non-renewable energy sources (fossil fuels), as well as an increase in environmental pollution.[200] Therefore, the development of new technologies, in which energy is obtained safely, cheaply, and without harming the environment is essential for the preservation of our society.

Among the energy conversion systems, electrochemical water splitting has proved to be very efficient when it comes to obtaining clean and high purity fuels.[201] In fact, from the electrochemical water splitting it is possible to obtain O_2 and H_2 through OER and HER that occur at the anode and cathode electrodes, respectively.[2,202]

The HER can be expressed depending on electrolyte pH, according to eqn (1) and (2):

$$\text{Acidic medium: } 2H^+ + 2e^- \rightarrow H_2 \quad (1)$$

$$\text{Neutral/alkaline medium: } 4H_2O + 4e^- \rightarrow 2H_2 + 4OH^- \quad (2)$$

In addition, the HER can be divided into two steps called Volmer and Heyrovsky or Tafel pathways, where H_{ads} acts as an intermediate species and plays a crucial role in the mechanism. The first step can proceed in acidic (eqn (3)) and neutral/alkaline solutions (eqn (4)), as indicated by the equations below:

$$H^+ + e^- \rightarrow H_{ads} \quad (3)$$

$$H_2O + e^- \rightarrow H_{ads} + OH^- \quad (4)$$

Depending on the coverage ratio of H_{ads} (θ_H), the second step can occur through Heyrovsky or Tafel pathways. Whereas the Heyrovsky pathway occurs due to low θ_H (eqn (5) in acidic medium and eqn (6) in neutral/alkaline medium), the Tafel pathway occurs in consequence of high θ_H, regardless of the pH value (eqn (7)).

$$H_{ads} + H^+ + e^- \rightarrow H_2 \quad (5)$$

$$H_2O + e^- + H_{ads} \rightarrow H_2 + OH^- \quad (6)$$

$$H_{ads} + H_{ads} \rightarrow H_2 \quad (7)$$

However, the obtaining of H_2 is limited by the sluggish reaction kinetics of the OER, because of the four-step electron transfer process ($4OH^- \rightarrow H_2O + O_2 + 4e^-$) in neutral or alkaline medium.

Currently, catalysts formed by using noble metals, such as RuO_2, IrO_2, and Pt, have been used in electrochemical water splitting in order to overcome the slow reaction kinetics of the OER.[203] However, these catalysts are scarce and expensive, and their use in industry is not feasible. Therefore, noble metal catalysts have been replaced by alternative ones such as layered double hydroxides,[2,204] oxides,[205,206] nitrides and sulfides,[207,208] and spinel structures.[209,210] Among these catalyst groups, spinel oxides with AB_2O_4 (A and B transition metals) in special $MnCo_2O_4$ have stood out as promising electrode materials for water splitting due to the ease of preparation, variable valence states and high redox stability in alkaline medium.[194]

The main $MnCo_2O_4$-based catalysts for the OER and HER are shown in Table 5. Most of the studies reported in the literature are related to the electrochemical performance of $MnCo_2O_4$ concerning the OER, and very few studies were found in the literature using $MnCo_2O_4$ as an electrocatalyst for the HER, suggesting that there is a vast unexplored field that deserves attention.

Despite advantages mentioned above, the catalytic activity of $MnCo_2O_4$ is limited by its low electrical conductivity. However, strategies have been explored in order to improve the electrical conductivity such as introduction of hetero-atoms, combining $MnCo_2O_4$ with conducting materials forming composites, incorporation of oxygen vacancies and nanoparticle size control.

In this sense, Rebekah and co-authors[211,212] showed that the catalytic activity of $MnCo_2O_4$ has been improved by the introduction of hetero-atoms (Ni and Zn), as well as by the combination of spinel oxide with rGO. Both Ni and Zn substituted $MnCo_2O_4$ on the rGO surface were synthesized through a hydrothermal method. The electrochemical behavior of $Mn_{1-x}Ni_xCo_2O_4$/rGO and $Mn_{1-x}Zn_xCo_2O_4$/rGO electrodes towards the OER was verified by Linear Sweep Voltammetry (LSV). Better results were achieved for the following compositions, $Mn_{0.4}Ni_{0.6}Co_2O_4$/rGO[211] (overpotential of 250 mV at 10 mA cm^{-2} and a Tafel slope of 78 mV dec^{-1}) and $Mn_{0.8}Zn_{0.2}Co_2O_4$/rGO[212] (overpotential of 320 mV at 10 mA cm^{-2} and a Tafel slope of 80.6 mV dec^{-1}). In summary, good electrochemical performance achieved by $Mn_{1-x}Ni_xCo_2O_4$/rGO and $Mn_{1-x}Zn_xCo_2O_4$/rGO electrodes towards the OER can be explained by the faster electron transport due to the more exposed active sites in consequence of the high surface area of rGO and of the reduction of metal ion aggregation owing to stacking between the sheets. In addition, the incorporation of another metallic ion resulted in a material with excellent electrochemical behavior and high conductivity.

The strategy of doping $MnCo_2O_4$ was also used by Huang *et al.*[213] in order to obtain an efficient electrocatalyst for both OER and HER. Indeed, the authors doped $MnCo_2O_4$ with Ce, being named as Ce–$MnCo_2O_4$. The OER and HER performances

Table 5 Catalytic activity parameters of recently reported HER/OER $MnCo_2O_4$-based electrocatalysts: overpotential at 10 mA cm^{-2}, onset potential, Tafel slope, stability, and pH condition[a]

	Catalysts	Substrate	Overpotential at 10 mA cm^{-2} (mV *vs.* RHE)	Onset potential (V *vs.* RHE)	Tafel slope (mV dec^{-1})	Stability (h)	pH condition	Ref.
OER catalysts	$MnCo_2O_4$@CoS NW	NF	280 at 20 mA cm^{-2}	1.51	139.19	10	1.0 M KOH	217
	$MnCo_2O_4$@CoS NS	NF	270 at 20 mA cm^{-2}	1.50	131.81	10	1.0 M KOH	217
	MCO/NS-MCS	NS-MCS	508	1.738	124	5.5	0.1 M KOH	21
	$MnCo_2O_4$	—	290	1.52	97	24	1.0 M KOH	193
	$MnCo_2O_4$@Mn–Co–P	Ti	269	1.50	102	100	1.0 M KOH	224
	$Mn_{1-x}Ni_xCo_2O_4$/rGO	CGE	250	1.48	78	2.8	1.0 M KOH	211
	$Mn_{1-x}Zn_xCo_2O_4$/rGO	GCE	320	1.48	80.6	2.8	1.0 M KOH	212
	YSM-MCO	NF	360	1.59	65.6	80	1.0 M KOH	225
	$MnCo_2O_4$@Ni_3S_2	NF	200 at 40 mA cm^{-2}	—	43.9	15	1.0 M KOH	226
	$MnCo_2O_4$/N-rmGO	GCE	330	1.56	—	—	1.0 M KOH	188
	$MnCo_2O_4$-rGO	GCE	530	1.56	106.9	—	0.1 M KOH	20
	$Mn_xCo_{3-x}O_4$	NF	327	—	79	25	1.0 M KOH	227
	$MnCo_2O_4$@Ni_2P	NF	240	—	114	30	1.0 M KOH	221
	$MnCo_2O_4$@NC	GCE	287	1.46	55	20	0.1 M KOH	218
	Ce–$MnCo_2O_4$	GCE	390	—	125	11.1	1.0 M KOH	213
	CMO/20N-rGO	GCE	450	1.68	80.2	8	0.1 M KOH	187
	Ce–$MnCo_2O_4$	GCE	389	—	96	12	1.0 M KOH	213
HER catalysts	$MnCo_2O_4$@Ni_2P	NF	57	—	89	20	1.0 M KOH	221
	NiFe–$MnCo_2O_4$/NFF	NFF	98	—	80.78	48	1.0 M KOH	19
	$MnCo_2O_4$@Ni_3S_2	NF	110	—	212.15	15	1.0 M KOH	226

[a] NW = nanowire; NF = nickel foam; NS = nanosheet; MCO = $MnCo_2O_4$; NS-MCS = nitrogen and sulfur co-doped mesoporous carbon spheres; rGO = reduced graphene oxide; GCE = glassy carbon electrode; YSM = yolk–shell; N-rmGO = N-doped reduced graphene oxide; NC = nitrogen doped carbon; CMO/20N-rGO = Co_3O_4–$MnCo_2O_4$/N-doped reduced graphene oxide with a mass ratio of NrGO/(Co + Mn) of *ca.* 20 wt%; NFF = Ni–Fe foam.

were evaluated by LSV and the material reached an overpotential of 390 and 379 mV, respectively. Those values when compared to $MnCo_2O_4$ without Ce doping are much superior. In fact, $MnCo_2O_4$ without Ce presented an overpotential at 10 mA cm^{-2} of 560 and 477 mV, respectively for the OER and HER. The OER results can be attributed to the introduction of Ce into $MnCo_2O_4$ that facilitates oxygen transfer through adsorption, dissociation and release of atomic O for the OER, besides the introduction of oxygen vacancies to dissociate water.[214–216]

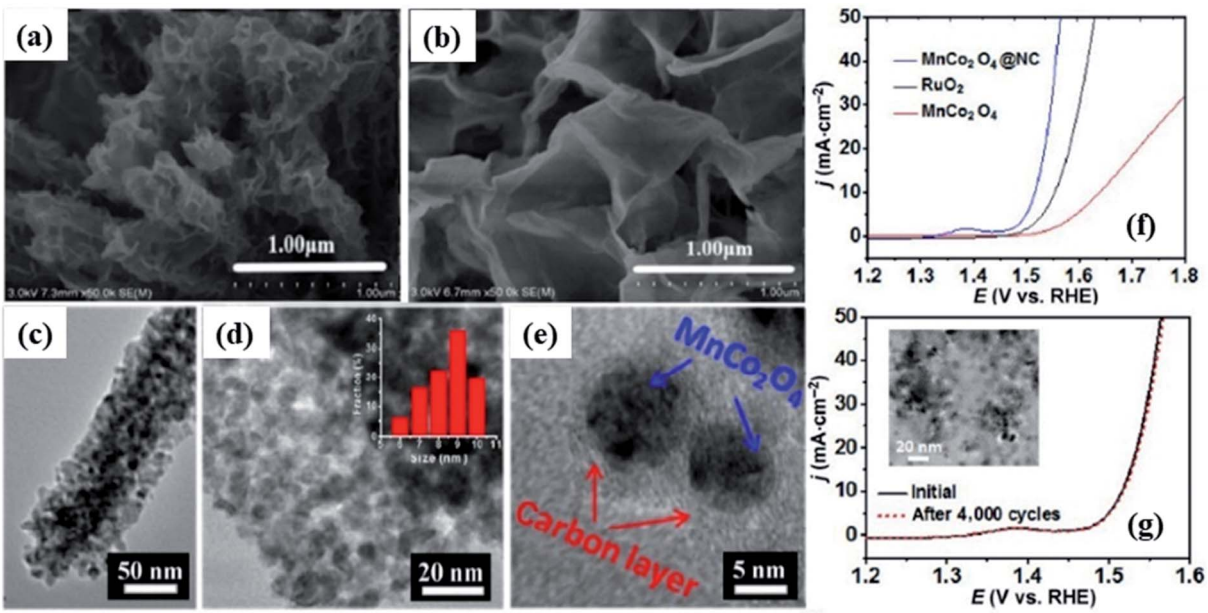

Fig. 10 TEM images of (a) $MnCo_2O_4$@CoS nanowires and (b) $MnCo_2O_4$@CoS nanosheets. Reproduced with permission from ref. 217. Copyright © 2019 Hydrogen Energy Publications LLC. Published by Elsevier Ltd. All rights reserved. (c, d) TEM and (e) HRTEM images of $MnCo_2O_4$@NC. (f) LSV curves of $MnCo_2O_4$@NC, RuO_2 and $MnCo_2O_4$ and (g) LSV initial curve and after 4000 curves for $MnCo_2O_4$@NC. Reproduced with permission from ref. 218. Copyright © 2016, Tsinghua University Press and Springer-Verlag Berlin Heidelberg.

Also, the electrical conductivity of $MnCo_2O_4$ can be improved through design of hierarchical 3D core@shell structures. Indeed, Du and co-authors[217] reported the synthesis of two materials based on $MnCo_2O_4$@CoS with different morphologies, using a hydrothermal method followed by the electrodeposition technique. As a matter of fact, $MnCo_2O_4$@CoS was synthesized in the nanowire and nanosheet shapes, as can be seen in TEM images displayed in Fig. 10a and b, respectively.

The electrocatalytic activity performances of $MnCo_2O_4$@CoS with different morphologies towards the OER are very similar, reaching 280 mV and 270 mV at 20 mA cm^{-2} for $MnCo_2O_4$@CoS nanowires and $MnCo_2O_4$@CoS nanosheets, respectively. Also, the surface areas of the materials were very similar as well. For $MnCo_2O_4$@CoS nanowires and $MnCo_2O_4$@CoS nanosheets the BET surface areas were 68.46 and 69.38 m^2 g^{-1}, respectively. Therefore, the electrochemical results cannot be attributed to the materials' surface area, but it can be related to the synergistic effect between $MnCo_2O_4$ and CoS, since the poor electrical conductivity of $MnCo_2O_4$ is compensated by the conductive CoS, and by the abundant oxygen vacancies. In fact, the existence of a large amount of oxygen vacancies can be estimated through XPS studies, where due to the co-existence of Co^{2+} and Co^{3+} ions the molar ratio of Co^{2+}/Co^{3+} is a good parameter to evaluate the oxygen vacancies. The molar ratio found for the $MnCo_2O_4$@CoS nanowires and $MnCo_2O_4$@CoS nanosheets was 0.88 and 0.93, respectively, indicating a large amount of oxygen vacancies.

Over the years, several studies have been reported in the literature where it is demonstrated that the size control of nanoparticles plays a key role in improving the properties of the materials. Using this strategy, Su *et al.*[218] encapsulated $MnCo_2O_4$ nanoparticles using nitrogen-doped carbon (NC), since the NC can not only act as an encapsulating agent controlling the growth of the nanoparticles but also improve the catalytic performance in water splitting.[219] The $MnCo_2O_4$ was encapsulated in NC, here denoted as $MnCo_2O_4$@NC from a metal–organic complex as a precursor, using a hydrothermal method. The TEM and HRTEM images of the as-prepared material are shown in Fig. 10c–e. It is possible to observe that the $MnCo_2O_4$@NC nanowires were made of several well-dispersed nanoparticles with less than 10 nm of average diameter (Fig. 10c). Besides, in Fig. 10e, the HRTEM image of $MnCo_2O_4$@NC is displayed, where it is clearly possible to observe that $MnCo_2O_4$ was encapsulated by NC, forming a core@shell structure. However, the $MnCo_2O_4$ nanowires without NC presented nanoparticles with an average diameter of 100 nm, demonstrating that the growth of $MnCo_2O_4$ nanoparticles was limited by the NC.

The results presented above can directly influence the catalytic activity of the material. The $MnCo_2O_4$@NC presented an electrochemical performance (overpotential of 287 mV at 10 mV cm^{-2} and Tafel slope of 55 mV dec^{-1}) far superior to that of $MnCo_2O_4$ nanowires (overpotential of ~420 mV at 10 mV cm^{-2} and Tafel slope of 101 mV dec^{-1}), Fig. 10f. Also, the $MnCo_2O_4$@NC did not show any change in the electrochemical profile after 4000 cycles, as can be seen in Fig. 10g. These results demonstrated that the size control of $MnCo_2O_4$ nanoparticles (less than 10 nm) using NP, in order to limit the growth of the nanoparticles, provided several active sites are exposed to oxygen adsorption and desorption. Besides, the nanoporous

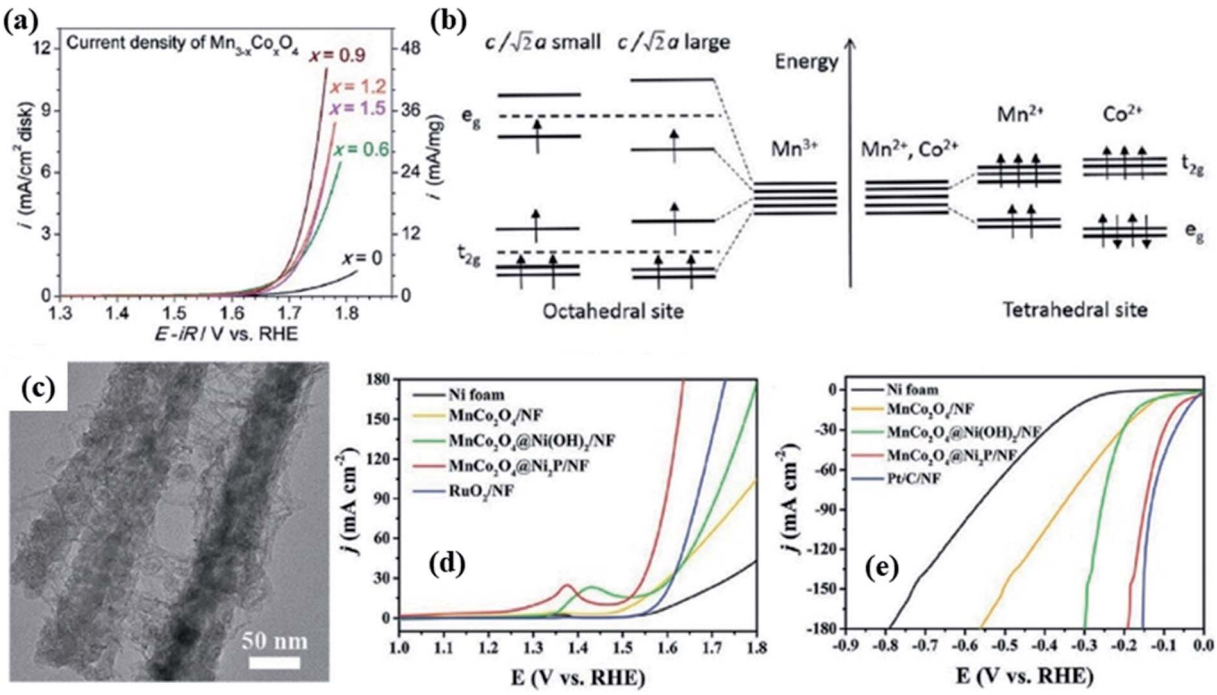

Fig. 11 LSV curves of different samples of $Mn_{3-x}Co_xO_4$ ($0 < x \leq 1.5$) (a) and schematic orbital energy diagram for Mn^{3+} 3d at octahedral sites and Mn^{2+} and Co^{2+} at tetrahedral sites (b). Reproduced with permission from ref. 220. Copyright © Marketplace™, Royal Society of Chemistry. TEM image of $MnCo_2O_4$@Ni_2P (c), LSV curves for the electrocatalytic performance of the OER (d) and HER (e). Reproduced with permission from ref. 221. Copyright © 2020 WILEY-VCH Verlag GmbH & Co. KGaA, Weinheim.

core@shell structure provided easy access of electrolyte ions and improved the electron transfer rate.

Recent studies have pointed out that one of the causes of the low catalytic activity and stability of Co-based compounds for water oxidation is the Jahn–Teller distortion. In this sense, Hirai *et al.*[220] performed a systematic study for tetragonal spinel oxides $Mn_{3-x}Co_xO_4$ ($0 \leq x < 1$ and $1 < x \leq 1.5$) in order to evaluate the relation between the Jahn–Teller distortion and catalytic activity for the OER. They figured out that for $Mn_{3-x}Co_xO_4$ ($0 \leq x < 1$) the catalytic activity was improved with the increase of Co concentration, due to the Jahn–Teller distortion suppression. However, for $Mn_{3-x}Co_xO_4$ ($1 < x \leq 1.5$) the OER activity decreased with Co concentration above 1 up to 1.5, when compared to $Mn_{3-x}Co_xO_4$ ($0 \leq x < 1$), as can be seen through LSV curves in Fig. 11a. Although Mn^{3+} still remains occupying the octahedral sites on the $Mn_{3-x}Co_xO_4$ ($0 \leq x < 1$), when cobalt is added it will occupy the tetrahedral sites, and thus the Jahn–Teller distortion is suppressed, represented by an indicator $c/\sqrt{2}a$ (Fig. 11b) and consequently there is an increase in catalytic activity, due to the strong interaction between the antibonding electron e_g and oxygen species adsorbed (O_2^{2-} and O^{2-}). Nevertheless, when the cobalt concentration is above >1, the octahedral sites are occupied by a mixture of Mn^{3+}, Co^{3+}, Mn^{4+}, and Co^{2+} ions and then the e_g orbital can be occupied by more than 1 electron or even not be occupied thus decreasing the catalytic activity.

Similarly, Ge *et al.*,[221] using an interface engineering strategy to suppress the Jahn–Teller distortion in $MnCo_2O_4$, grew Ni_2P nanosheets on the $MnCo_2O_4$ surface obtaining a bifunctional catalyst for the OER and HER. The $MnCo_2O_4$@Ni_2P was obtained in four steps. The precursor MnCo-LDH was obtained through the hydrothermal method, and then the as-precursor MnCo-LDH was annealed in order to obtain $MnCo_2O_4$. A second hydrothermal method was used to deposit $Ni(OH)_2$ nanosheets on $MnCo_2O_4$. After that, the $MnCo_2O_4$@$Ni(OH)_2$ was calcined in the presence of NaH_2PO_2 in order to obtain $MnCo_2O_4$@Ni_2P. In Fig. 11c the TEM image of $MnCo_2O_4$@Ni_2P is displayed, where it is possible to observe that the $MnCo_2O_4$ nanoneedles are coated by a large number of Ni_2P nanosheets.

The electrochemical performance of $MnCo_2O_4$@Ni_2P towards the OER and HER was evaluated by LSV, and the curves are shown in Fig. 11d and e. The hierarchical $MnCo_2O_4$@Ni_2P structure exhibited an excellent overpotential for the OER (240 mV at 10 mA cm^{-2}) and a Tafel slope of 114 mV dec^{-1}. Also, the $MnCo_2O_4$@Ni_2P showed an outstanding HER performance with an overpotential of 10 mA cm^{-2} (57 mV) and a Tafel slope of 89 mV dec^{-1}. This HER performance can be explained by the presence of several Ni^0 and Ni^{2+} species, as determined by XPS after phosphorization, once those species can provide energy in order to stabilize the H_{ads} through the weakening of the O–H bond of adsorbed water.[222]

The electronic interactions between $MnCo_2O_4$ and Ni_2P were clarified through differential charge density. The high charge density is placed on the Ni_2P side, and thus the electrons migrate from Ni_2P to $MnCo_2O_4$ due to the strong interfacial polarization.[223] Thus, the strong interaction between $MnCo_2O_4$@Ni_2P reduces the Jahn–Teller distortion and the Ni_2P with metallic properties increases the electronic conductivity and charge transfer rate of $MnCo_2O_4$@Ni_2P.

5. Conclusions and future directions

Lately spinel $MnCo_2O_4$-based materials have stood out in the energy conversion and storage technologies, especially due to their low cost, simple preparation and chemical composition versatility obtained through different strategies that enabled the rational design of these materials, thus allowing tuning of their electronic properties. In addition, reducing Co ions in the structure of Co_3O_4 by replacing them with Mn ions has been an excellent strategy to increase the conductivity and improve the electrochemical performance of the electrode materials. In fact, studies have shown that the conductivity of $MnCo_2O_4$ is greater than that of Co_3O_4, and its electrochemical performance is superior since Co provides a higher oxidation potential than Mn and Mn brings a higher capacity than Co owing to its efficient electron transport.[115] Thus, the recent advances have been summarized in this review and special emphasis was directed to spinel $MnCo_2O_4$ based materials, which are highly promising for the construction of supercapacitors and batteries, and thus the development of arrangements for water-splitting for energy conversion. It is necessary to highlight that the application of $MnCo_2O_4$ as a multifunctional material still needs fine control of synthesis conditions, which will impact the phase, morphology, cation distribution, and especially the electrical properties, and it is an important requirement for energy applications.

The construction of supercapacitors using $MnCo_2O_4$ in the pristine form or as composites based on metal oxides/hydroxides, polymers or carbon-based composites or other materials was described as an important strategy to increase the capacitance and rate capability of hybrid devices, resulting in supercapacitors with higher energy and power density.

Additionally, LIBs, SIBs and metal–O_2 batteries are also covered. In order to improve the electrochemical performance in LIBs, in addition to developing composites of $MnCo_2O_4$ with other materials, morphological modifications and synthesis methods have been the focus of researchers, particularly on the preparation of porous materials (mesoporous, hollow, yolk–shell, shell-in-shell, and yolk-in-double-shell spheres). Mesoporous transition metal-doped $MnCo_2O_4$ has also been reported for application in SIBs, while heteroatoms doped-carbon materials were mixed with $MnCo_2O_4$ due to intrinsic advantages as ORR catalysts, such as high surface area and electrochemical stability in metal–O_2 batteries. The results obtained with $MnCo_2O_4$ for the construction of supercapacitors, metal-ion batteries, and metal–air batteries were tabulated.

Conversely, $MnCo_2O_4$ based materials showed great potential as electrocatalysts in energy storage devices. For instance, conductivity optimization by the formation of composites with conducting carbon materials has been the main strategy for preparing excellent electrocatalysts for the ORR (or bifunctional electrocatalysts for the OER/ORR). However, porous spinels with tunable size, shape, chemical composition and crystalline structure were also reported *via* a facile precursor pyrolysis method.

$MnCo_2O_4$ was also recently used as an electrocatalyst for energy conversion, mainly in water splitting. Most of the studies reported in the literature are related to the electrochemical performance of $MnCo_2O_4$ concerning the OER, and very few studies were found in the literature using $MnCo_2O_4$ as an electrocatalyst for the HER, suggesting that there is a vast unexplored field that deserves attention. Thereunto, strategies have been explored in order to improve the electrical conductivity and electrocatalytic activity, such as introduction of hetero-atoms (or doping), combination with conducting materials forming composites, incorporation of oxygen vacancies and nanoparticle size control.

As demonstrated in this article, the utilization of spinel $MnCo_2O_4$-based materials for energy storage and conversion is a promising new concept in energy technologies. It is also important to highlight that future research should continue to enrich spinel $MnCo_2O_4$-based materials, focusing attention on the electrochemical performance and reasonable architectural design of those materials for practical application in energy technologies and expanding the fields of application. In fact, it is possible to visualize a field still unexplored and of great potential for application, for instance, the rational design of different composite materials composed of $MnCo_2O_4$ and/or heterojunctions containing the recent advanced 2D materials (such as MXene, transition metal chalcogenides, black phosphorus, *etc.*), aiming at future applications of these supercapacitor/battery materials for flexible/wearable devices, self-charged energy storage devices, and microsupercapacitors. The future applications of flexible/wearable energy devices depend on suitable flexible substrates that can stably and efficiently incorporate $MnCo_2O_4$ or its composites. In this direction, novel current collectors have been investigated and carbon cloth has shown promising results due to its excellent flexibility and conductivity. Additionally, different synthesis strategies urge investigation, and in this sense, electrochemical growth on flexible conductive substrates is promising (without binders and using a simplified rotocol). Considering large-scale and reproducible production, additive manufacturing (or three-dimensional printing) protocols offer great promise in this area.

Moreover, bifunctional and multifunctional catalysts represent promising directions,[15] especially for electrocatalysts for water splitting (HER/OER) and metal–air batteries (ORR/OER). Other applications, such as the use of $MnCo_2O_4$ catalysts to convert greenhouse gases (CO_2) and toxic gas (CO) into chemical fuels, are also feasible. From this perspective, $MnCo_2O_4$-based materials have a key role in the way to a more sustainable society and industrial applications.

Conflicts of interest

The authors declare that there is no conflict of interest.

Acknowledgements

This work was supported by the Sao Paulo Research Foundation (FAPESP processes 2018/16896-7, 2017/13137-5 and 2020/00325-0), the National Council for Scientific and Technological Development (CNPq Processes 307271/2017-0 and 311847/2018-8), Coordination for the Improvement of Higher Education Personnel (CAPES) Financial code 001 and to Brazilian Institute of Science and Technology in Bioanalytics (INCTBio) (CNPq grant no. 465389/2014-7 and FAPESP grant no. 2014/50867-3) and Brazilian Institute of Science and Technology (INCT) in Carbon Nanomaterials. CSR acknowledges the Department of Science and Technology (DST)-SERB Early Career Research project (Grant No. ECR/2017/001850), DST-Nanomission (DST/NM/NT/2019/205(G)) and Karnataka Science and Technology Promotion Society (KSTePS/VGST-RGS-F/2018-19/GRD NO. 829/315).

References

1 S. Ghosh and R. N. Basu, *Nanoscale*, 2018, **10**, 11241–11280.
2 J. M. Gonçalves, P. R. Martins, L. Angnes and K. Araki, *New J. Chem.*, 2020, **44**, 9981–9997.
3 J. M. Gonçalves, T. A. Matias, K. C. F. Toledo and K. Araki, in *Advances in Inorganic Chemistry*, ed. R. V. Eldik and C. Hubbard, Elsevier, 2019, vol. 74, p. 63.
4 J. Xu, C. Chen, Z. Han, Y. Yang, J. Li and Q. Deng, *Nanomaterials*, 2019, **9**, 1161.
5 J. M. Gonçalves, M. I. da Silva, H. E. Toma, L. Angnes, P. R. Martins and K. Araki, *J. Mater. Chem. A*, 2020, **8**, 10534–10570.
6 S. J. Uke, V. P. Akhare, D. R. Bambole, A. B. Bodade and G. N. Chaudhari, *Front. Mater.*, 2017, **4**, 21.
7 X. Wang, A. Hu, C. Meng, C. Wu, S. Yang and X. Hong, *Molecules*, 2020, **25**, 269.
8 Y. Shi, X. Pan, B. Li, M. Zhao and H. Pang, *Chem. Eng. J.*, 2018, **343**, 427–446.
9 X. Hu, L. Wei, R. Chen, Q. Wu and J. Li, *ChemistrySelect*, 2020, **5**, 5268–5288.
10 M. Hamdani, R. N. Singh and P. Chartier, *Int. J. Electrochem. Sci.*, 2010, **5**, 556–577.
11 J. Zhu, Q. Wu and J. Li, *ChemistrySelect*, 2020, **5**, 10407–10423.
12 A. U. Ubale, M. A. Waghmare, K. S. Iqbal and H. M. Pathan, *J. Mater. Sci.: Mater. Electron.*, 2020, **31**, 14003–14021.
13 L. Tian, X. Zhai, X. Wang, J. Li and Z. Li, *J. Mater. Chem. A*, 2020, **8**, 14400–14414.
14 X. Zhao, L. Mao, Q. Cheng, J. Li, F. Liao, G. Yang, L. Xie, C. Zhao and L. Chen, *Chem. Eng. J.*, 2020, **387**, 124081.
15 Y. Li, X. Han, T. Yi, Y. He and X. Li, *J. Energy Chem.*, 2019, **31**, 54–78.
16 J. P. Cheng, W. D. Wang, X. C. Wang and F. Liu, *Chem. Eng. J.*, 2020, **393**, 124747.
17 X. Han, X. Gui, T.-F. Yi, Y. Li and C. Yue, *Curr. Opin. Solid State Mater. Sci.*, 2018, **22**, 109–126.
18 R. Kumar, *Nano-Micro Lett.*, 2020, **12**, 122.
19 Y. Lin, Z. Yang, D. Cao and Y. Gong, *Crystengcomm*, 2020, **22**, 1425–1435.
20 H. Yang, M. Zhu, X. Guo, C. Yan and S. Lin, *ACS Omega*, 2019, **4**, 22325–22331.
21 T. Oh, S. Ryu, H. Oh and J. Kim, *Dalton Trans.*, 2019, **48**, 945–953.

22 S. Yuvaraj, A. Vignesh, S. Shanmugam and R. Kalai Selvan, *Int. J. Hydrogen Energy*, 2016, **41**, 15199–15207.
23 Y. Li, M. S. Wu and C. Y. Ouyang, *Appl. Surf. Sci.*, 2015, **349**, 510–515.
24 N. R. Chodankar, H. D. Pham, A. K. Nanjundan, J. F. S. Fernando, K. Jayaramulu, D. Golberg, Y.-K. Han and D. P. Dubal, *Small*, 2020, **16**, 2002806.
25 Y. Gogotsi and R. M. Penner, *ACS Nano*, 2018, **12**, 2081–2083.
26 V. Sannasi and K. Subbian, *Ceram. Int.*, 2020, **46**, 15510–15520.
27 S. G. Krishnan, M. H. A. Rahim and R. Jose, *J. Alloys Compd.*, 2016, **656**, 707–713.
28 H. Liu, X. Liu, S. Wang, H.-K. Liu and L. Li, *Energy Storage Mater.*, 2020, **28**, 122–145.
29 S. Liu, D. Ni, H.-F. Li, K. N. Hui, C.-Y. Ouyang and S. C. Jun, *J. Mater. Chem. A*, 2018, **6**, 10674–10685.
30 H. Adhikari, D. Neupane, C. K. Ranaweera, J. Candler, R. K. Gupta, S. Sapkota, X. Shen and S. R. Mishra, *Electrochim. Acta*, 2017, **225**, 514–524.
31 S. Al-Rubaye, R. Rajagopalan, C. M. Subramaniyam, Z. Yu, S. X. Dou and Z. Cheng, *J. Power Sources*, 2016, **324**, 179–187.
32 R. BoopathiRaja and M. Parthibavarman, *J. Alloys Compd.*, 2019, **811**, 152084.
33 K. R. Shrestha, S. Kandula, N. H. Kim and J. H. Lee, *J. Alloys Compd.*, 2019, **771**, 810–820.
34 Y. Zhang, L. Li, H. Su, W. Huang and X. Dong, *J. Mater. Chem. A*, 2015, **3**, 43–59.
35 A. K. Mondal, D. Su, S. Chen, A. Ung, H.-S. Kim and G. Wang, *Chem.–Eur. J.*, 2015, **21**, 1526–1532.
36 Y. Gao, Y. Xia, H. Wan, X. Xu and S. Jiang, *Electrochim. Acta*, 2019, **301**, 294–303.
37 L.-B. Kong, C. Lu, M.-C. Liu, Y.-C. Luo, L. Kang, X. Li and F. C. Walsh, *Electrochim. Acta*, 2014, **115**, 22–27.
38 K. N. Hui, K. S. Hui, Z. Tang, V. V. Jadhav and Q. X. Xia, *J. Power Sources*, 2016, **330**, 195–203.
39 J. Xu, Y. Sun, M. Lu, L. Wang, J. Zhang, E. Tao, J. Qian and X. Liu, *Acta Mater.*, 2018, **152**, 162–174.
40 V. Venkatachalam, A. Alsalme, A. Alghamdi and R. Jayavel, *J. Electroanal. Chem.*, 2015, **756**, 94–100.
41 M. Li, W. Yang, J. Li, M. Feng, W. Li, H. Li and Y. Yu, *Nanoscale*, 2018, **10**, 2218–2225.
42 J. Li, D. Xiong, L. Wang, M. K. S. Hirbod and X. Li, *J. Energy Chem.*, 2019, **37**, 66–72.
43 S. Nagamuthu, S. Vijayakumar, S.-H. Lee and K.-S. Ryu, *Appl. Surf. Sci.*, 2016, **390**, 202–208.
44 S. Sahoo, K. K. Naik and C. S. Rout, *Nanotechnology*, 2015, **26**, 455401.
45 Y. Dong, Y. Wang, Y. Xu, C. Chen, Y. Wang, L. Jiao and H. Yuan, *Electrochim. Acta*, 2017, **225**, 39–46.
46 M. A. Akhtar, V. Sharma, S. Biswas and A. Chandra, *RSC Adv.*, 2016, **6**, 96296–96305.
47 Z. Liu, F. Teng, C. Yuan, Z. Ul Abideen, W. Gu and Z. Liu, *Energy Technol.*, 2019, **7**, 1900314.
48 T. Huang, C. Zhao, L. Wu, X. Lang, K. Liu and Z. Hu, *Ceram. Int.*, 2017, **43**, 1968–1974.
49 M. Shanmugavadivel, V. V. Dhayabaran and M. Subramanian, *J. Phys. Chem. Solids*, 2019, **133**, 15–20.
50 L. Li, Y. Q. Zhang, X. Y. Liu, S. J. Shi, X. Y. Zhao, H. Zhang, X. Ge, G. F. Cai, C. D. Gu, X. L. Wang and J. P. Tu, *Electrochim. Acta*, 2014, **116**, 467–474.
51 Y. Xu, X. Wang, C. An, Y. Wang, L. Jiao and H. Yuan, *J. Mater. Chem. A*, 2014, **2**, 16480–16488.
52 Q. Wang, X. Wang, B. Liu, G. Yu, X. Hou, D. Chen and G. Shen, *J. Mater. Chem. A*, 2013, **1**, 2468–2473.
53 L. Zhao, M. Yang, Z. Zhang, Y. Ji, Y. Teng, Y. Feng and X. Liu, *Inorg. Chem. Commun.*, 2018, **89**, 22–26.
54 J.-J. Zhou, X. Han, K. Tao, Q. Li, Y.-L. Li, C. Chen and L. Han, *Chem. Eng. J.*, 2018, **354**, 875–884.
55 Y. Lv, A. Liu, H. Che, J. Mu, Z. Guo, X. Zhang, Y. Bai, Z. Zhang, G. Wang and Z. Pei, *Chem. Eng. J.*, 2018, **336**, 64–73.
56 T. Chen, R. Shi, Y. Zhang and Z. Wang, *ChemPlusChem*, 2019, **84**, 69–77.
57 J. A.-A. Mehrez, K. A. Owusu, Q. Chen, L. Li, K. Hamwi, W. Luo and L. Mai, *Inorg. Chem. Front.*, 2019, **6**, 857–865.
58 K. R. Shrestha, S. Kandula, G. Rajeshkhanna, M. Srivastava, N. H. Kim and J. H. Lee, *J. Mater. Chem. A*, 2018, **6**, 24509–24522.
59 S. Liu, K. S. Hui and K. N. Hui, *ChemNanoMat*, 2015, **1**, 593–602.
60 X. Zheng, Y. Ye, Q. Yang, B. Geng and X. Zhang, *Dalton Trans.*, 2016, **45**, 572–578.
61 Y. Zhang, H. Xuan, Y. Xu, B. Guo, H. Li, L. Kang, P. Han, D. Wang and Y. Du, *Electrochim. Acta*, 2016, **206**, 278–290.
62 M. Harilal, S. G. Krishnan, A. Yar, I. I. Misnon, M. V. Reddy, M. M. Yusoff, J. Ojur Dennis and R. Jose, *J. Phys. Chem. C*, 2017, **121**, 21171–21183.
63 X. Guo, M. Li, Y. Liu, Y. Huang, S. Geng, W. Yang and Y. Yu, *J. Colloid Interface Sci.*, 2020, **563**, 405–413.
64 V. V. M. Chandu, Gopi, M. Venkata-Haritha, S.-K. Kim, K. Prabakar and H.-J. Kim, *RSC Adv.*, 2016, **6**, 102961–102967.
65 B. Cheng, W. Zhang, M. Yang, Y. Zhang and F. Meng, *Ceram. Int.*, 2019, **45**, 20451–20457.
66 F. Liao, X. Han, Y. Zhang, X. Han, C. Xu and H. Chen, *Ceram. Int.*, 2019, **45**, 7244–7252.
67 S. Liu, K. San Hui, K. N. Hui, J. M. Yun and K. H. Kim, *J. Mater. Chem. A*, 2016, **4**, 8061–8071.
68 H.-M. Lee, C. V. V. Muralee Gopi, P. J. S. Rana, R. Vinodh, S. Kim, R. Padma and H.-J. Kim, *New J. Chem.*, 2018, **42**, 17190–17194.
69 Y. Feng, W. Liu, L. Sun, Y. Zhu, Y. Chen, M. Meng, J. Li, J. Yang, Y. Zhang and K. Liu, *J. Alloys Compd.*, 2018, **753**, 761–770.
70 L. Yu, G. Zhang, C. Yuan and X. W. Lou, *Chem. Commun.*, 2013, **49**, 137–139.
71 J. Yang, Y. Liu, S. Liu, L. Li, C. Zhang and T. Liu, *Mater. Chem. Front.*, 2017, **1**, 251–268.
72 F. Wang, X. Lv, L. Zhang, H. Zhang, Y. Zhu, Z. Hu, Y. Zhang, J. Ji and W. Jiang, *J. Power Sources*, 2018, **393**, 169–176.
73 P. Hu, D. Zhao, H. Liu, K. Chen and X. Wu, *CrystEngComm*, 2019, **21**, 1600–1606.

74 S. Abouali, M. Akbari Garakani, Z.-L. Xu and J.-K. Kim, *Carbon*, 2016, **102**, 262–272.
75 L. L. Zhang and X. S. Zhao, *Chem. Soc. Rev.*, 2009, **38**, 2520–2531.
76 H. Wang, C. Shen, J. Liu, W. Zhang and S. Yao, *J. Alloys Compd.*, 2019, **792**, 122–129.
77 D. Wu, H. Han, X. Hong, S. Tao, S. Xu, B. Qian, L. Wang, X. Chen and P. K. Chu, *J. Alloys Compd.*, 2020, **846**, 155720.
78 X. Hu, H. Nan, M. Liu, S. Liu, T. An and H. Tian, *Electrochim. Acta*, 2019, **306**, 599–609.
79 L. Li, F. He, S. Gai, S. Zhang, P. Gao, M. Zhang, Y. Chen and P. Yang, *CrystEngComm*, 2014, **16**, 9873–9881.
80 T. T. Gebremariam, F. Chen, Q. Wang, J. Wang, Y. Liu, X. Wang and A. Qaseem, *ACS Appl. Energy Mater.*, 2018, **1**, 1612–1625.
81 P. Hao, Z. Zhao, L. Li, C.-C. Tuan, H. Li, Y. Sang, H. Jiang, C. P. Wong and H. Liu, *Nanoscale*, 2015, **7**, 14401–14412.
82 T. Pettong, P. Iamprasertkun, A. Krittayavathananon, P. Sukha, P. Sirisinudomkit, A. Seubsai, M. Chareonpanich, P. Kongkachuichay, J. Limtrakul and M. Sawangphruk, *ACS Appl. Mater. Interfaces*, 2016, **8**, 34045–34053.
83 Y. Zhu, C. Zhang, S. Tang, H. Huang, S. Wang, Q. Luo and Y. Du, *ACS Appl. Energy Mater.*, 2019, **2**, 7546–7553.
84 M. Zhang, W. Liu, R. Liang, R. Tjandra and A. Yu, *Sustainable Energy Fuels*, 2019, **3**, 2499–2508.
85 P. Saren, A. De Adhikari, S. Khan and G. C. Nayak, *J. Solid State Chem.*, 2019, **271**, 282–291.
86 G. Liu, B. Wang, T. Liu, L. Wang, H. Luo, T. Gao, F. Wang, A. Liu and D. Wang, *J. Mater. Chem. A*, 2018, **6**, 1822–1831.
87 S. G. Mohamed, T.-F. Hung, C.-J. Chen, C. K. Chen, S.-F. Hu and R.-S. Liu, *RSC Adv.*, 2014, **4**, 17230–17235.
88 C. Xiao, X. Zhang and D. R. MacFarlane, *Electrochim. Acta*, 2018, **280**, 55–61.
89 N. Cai, J. Fu, V. Chan, M. Liu, W. Chen, J. Wang, H. Zeng and F. Yu, *J. Alloys Compd.*, 2019, **782**, 251–262.
90 Y. Ji, J. Xie, J. Wu, Y. Yang, X.-Z. Fu, R. Sun and C.-P. Wong, *J. Power Sources*, 2018, **393**, 54–61.
91 H. Che, Y. Lv, A. Liu, H. Li, Z. Guo, J. Mu, Y. Wang and X. Zhang, *Chem. Eng. J.*, 2020, **384**, 123372.
92 Y. Zhao, L. Hu, S. Zhao and L. Wu, *Adv. Funct. Mater.*, 2016, **26**, 4085–4093.
93 Y. Lv, Z. Guo, A. Liu, H. Che, J. Mu, X. Zhang, Y. Bai, Z. Zhang and G. Wang, *Ceram. Int.*, 2017, **43**, 12948–12956.
94 Y. Lv, A. Liu, Z. Shi, J. Mu, Z. Guo, X. Zhang and H. Che, *ChemElectroChem*, 2018, **5**, 3968–3979.
95 W. Li, K. Xu, G. Song, X. Zhou, R. Zou, J. Yang, Z. Chen and J. Hu, *CrystEngComm*, 2014, **16**, 2335–2339.
96 A. Krittayavathananon, T. Pettong, P. Kidkhunthod and M. Sawangphruk, *Electrochim. Acta*, 2017, **258**, 1008–1015.
97 S. Li, J. Wang, M. Wang and Y. Ni, *CrystEngComm*, 2019, **21**, 403–410.
98 H. Che, A. Liu, J. Mu, C. Wu and X. Zhang, *Ceram. Int.*, 2016, **42**, 2416–2424.
99 H. Che, Y. Wang and Y. Mao, *J. Alloys Compd.*, 2016, **680**, 586–594.
100 M. Haripriya, A. M. Ashok, S. Hussain and R. Sivasubramanian, *Ionics*, 2020, DOI: 10.1007/s11581-020-03788-y.
101 H. Liu, Z. Guo, S. Wang, X. Xun, D. Chen and J. Lian, *J. Alloys Compd.*, 2020, **846**, 156504.
102 Y. Zhai, H. Mao, P. Liu, X. Ren, L. Xu and Y. Qian, *J. Mater. Chem. A*, 2015, **3**, 16142–16149.
103 N. Mohamed and N. K. Allam, *RSC Adv.*, 2020, **10**, 21662–21685.
104 M. M. S. Sanad, A. K. Yousef, M. M. Rashad, A. H. Naggar and A. Y. El-Sayed, *Phys. B*, 2020, **579**, 411889.
105 X. Wu, S. Li, B. Wang, J. Liu and M. Yu, *New J. Chem.*, 2015, **39**, 8416–8423.
106 C. Fu, G. Li, D. Luo, X. Huang, J. Zheng and L. Li, *ACS Appl. Mater. Interfaces*, 2014, **6**, 2439–2449.
107 D. Darbar, M. R. Anilkumar, V. Rajagopalan, I. Bhattacharya, H. I. Elim, T. Ramakrishnappa, F. I. Ezema, R. Jose and M. V. Reddy, *Ceram. Int.*, 2018, **44**, 4630–4639.
108 S. Zhou, X. Luo, L. Chen, C. Xu and D. Yan, *Ceram. Int.*, 2018, **44**, 17858–17863.
109 Y. Zhang, X. Wang, Q. Zhao, Y. Fu, H. Wang and H. Shu, *Electrochim. Acta*, 2015, **180**, 866–872.
110 L. Zhang, Q. Tang, X. Chen, B. Fan, K. Xiao, S. Zhang, W. Deng and A. Hu, *J. Alloys Compd.*, 2017, **722**, 387–393.
111 M. V. Reddy, Y. Xu, V. Rajarajan, T. Ouyang and B. V. R. Chowdari, *ACS Sustainable Chem. Eng.*, 2015, **3**, 3035–3042.
112 G. Li, Q. Zhai, Q. Liu and R. Jin, *Cryst. Res. Technol.*, 2017, **52**, 1600255.
113 J. Qi, P. Wang, Y. Yan, X. Zheng, J. Cao and J. Feng, *Vacuum*, 2019, **169**, 108959.
114 D. S. Baji, H. S. Jadhav, S. V. Nair and A. K. Rai, *J. Solid State Chem.*, 2018, **262**, 191–198.
115 G. Li, L. Xu, Y. Zhai and Y. Hou, *J. Mater. Chem. A*, 2015, **3**, 14298–14306.
116 X. Hou, X. Wang, B. Liu, Q. Wang, T. Luo, D. Chen and G. Shen, *Nanoscale*, 2014, **6**, 8858–8864.
117 T. Huang, Z. Lou, Y. Lu, R. Li, Y. Jiang, G. Shen and D. Chen, *ChemElectroChem*, 2019, **6**, 5836–5843.
118 L. Ni, W. Tang, X. Liu, N. Zhang, J. Wang, S. Liang, R. Ma and G. Qiu, *Dalton Trans.*, 2018, **47**, 3775–3784.
119 F. Yang, W. Li and B. Tang, *Chem. Eng. J.*, 2018, **334**, 2021–2029.
120 J. Li, J. Wang, X. Liang, Z. Zhang, H. Liu, Y. Qian and S. Xiong, *ACS Appl. Mater. Interfaces*, 2014, **6**, 24–30.
121 G. Huang, S. Xu, Y. Yang, H. Sun and Z. Xu, *RSC Adv.*, 2016, **6**, 10763–10774.
122 R. Jin, Y. Ma, Y. Sun, H. Li, Q. Wang and G. Chen, *Energy Technol.*, 2017, **5**, 293–299.
123 J. Li, S. Xiong, X. Li and Y. Qian, *Nanoscale*, 2013, **5**, 2045–2054.
124 H. Yang, Y. Xie, M. Zhu, Y. Liu, Z. Wang, M. Xu and S. Lin, *Dalton Trans.*, 2019, **48**, 9205–9213.
125 Y. Jin, L. Wang, Q. Jiang, X. Du, C. Ji and X. He, *Mater. Lett.*, 2016, **177**, 85–88.

126 H. Xu, H. Shen, X. Song, X. Kong, Y. Zhang and Z. Qin, *J. Electroanal. Chem.*, 2019, **851**, 113455.
127 X. Kong, T. Zhu, F. Cheng, M. Zhu, X. Cao, S. Liang, G. Cao and A. Pan, *ACS Appl. Mater. Interfaces*, 2018, **10**, 8730–8738.
128 G. Huang, S. Xu, Z. Xu, H. Sun and L. Li, *ACS Appl. Mater. Interfaces*, 2014, **6**, 21325–21334.
129 J. Zhu, G. Cao, Y. Zhou, Y. Li, J. Zheng and D. Zhang, *ChemSusChem*, 2020, **13**, 1890–1899.
130 T. Li, X. Li, Z. Wang, H. Guo, Q. Hu and W. Peng, *Electrochim. Acta*, 2016, **191**, 392–400.
131 M. Wang, X. Yu, L. Hou, A. Gagnoud, Y. Fautrelle, R. Moreau and X. Li, *Chem. Eng. J.*, 2018, **351**, 930–938.
132 A. F. Shaikh, R. S. Kalubarme, M. S. Tamboli, S. S. Patil, M. V. Kulkarni, D. R. Patil, S. W. Gosavi, C.-J. Park and B. B. Kale, *ChemistrySelect*, 2017, **2**, 4630–4637.
133 L. Wu, J. Lang, S. Wang, P. Zhang and X. Yan, *Electrochim. Acta*, 2016, **203**, 128–135.
134 Y. Zhu, Y. Huang and M. Wang, *Chem. Eng. J.*, 2019, **378**, 122207.
135 R. Ding, Z. Li, C. Wang and M. Chen, *J. Alloys Compd.*, 2017, **726**, 445–452.
136 P. Huang, M. Zhao, B. Jin, H. Li, Z. Zhu, L. Jiang and Q. Jiang, *Dalton Trans.*, 2018, **47**, 14540–14548.
137 P. Zhang, J. Liu, J. Wu, W. Wang, C. Zhou, S. Guo, S. Li, Y. Yang and L. Chen, *Mater. Today Energy*, 2020, **17**, 100451.
138 C. Chen, B. Liu, Q. Ru, S. Ma, B. An, X. Hou and S. Hu, *J. Power Sources*, 2016, **326**, 252–263.
139 G. Huang, X. Guo, X. Cao, Q. Tian and H. Sun, *J. Alloys Compd.*, 2017, **695**, 2937–2944.
140 P. Kulkarni, D. Ghosh, G. Balakrishna, R. S. Rawat, S. Adams and M. V. Reddy, *Ceram. Int.*, 2019, **45**, 10619–10625.
141 R. Jin, Y. Meng, Y. Ma, H. Li, Y. Sun and G. Chen, *Electrochim. Acta*, 2016, **209**, 163–170.
142 L.-Q. Fan, J.-L. Huang, Y.-L. Wang, C.-L. Geng, S.-J. Sun, Y.-F. Huang and J.-H. Wu, *J. Energy Storage*, 2020, **30**, 101427.
143 P. Huang, F. Xu, G. Zhu, C. Dong, B. Jin, H. Li and Q. Jiang, *ChemPlusChem*, 2019, **84**, 1596–1603.
144 L. Wu, J. Lang, P. Zhang, X. Zhang, R. Guo and X. Yan, *J. Mater. Chem. A*, 2016, **4**, 18392–18400.
145 X. Wu, W. Wu, K. Wang, W. Chen and D. He, *Mater. Lett.*, 2015, **147**, 85–87.
146 M. Islam, M. Akbar, G. Ali, K.-W. Nam, K. Y. Chung and H.-G. Jung, *Ceram. Int.*, 2020, **46**, 26147–26155.
147 L. Zhu, F. Li, T. Yao, T. Liu, J. Wang, Y. Li, H. Lu, R. Qian, Y. Liu and H. Wang, *Energy Fuels*, 2020, **34**, 11574–11580.
148 L. Hou, S. Deng, Y. Jiang, R. Cui, Y. Zhou, Y. Guo, J. Li and F. Gao, *Nanotechnology*, 2020, **31**, 375404.
149 M. A. Rahman, X. Wang and C. Wen, *J. Appl. Electrochem.*, 2014, **44**, 5–22.
150 R. S. Kalubarme, H. S. Jadhav, D. T. Ngo, G.-E. Park, J. G. Fisher, Y.-I. Choi, W.-H. Ryu and C.-J. Park, *Sci. Rep.*, 2015, **5**, 13266.
151 S. G. Mohamed, Y.-Q. Tsai, C.-J. Chen, Y.-T. Tsai, T.-F. Hung, W.-S. Chang and R.-S. Liu, *ACS Appl. Mater. Interfaces*, 2015, **7**, 12038–12046.
152 K. Song, L. Yuan, Z. Li, Y. Lv, B. Yang, Y. Yu, X. Shen and X. Hu, *Electrochim. Acta*, 2020, **353**, 136572.
153 H. Wu, W. Sun, Y. Wang, F. Wang, J. Liu, X. Yue, Z. Wang, J. Qiao, D. W. Rooney and K. Sun, *ACS Appl. Mater. Interfaces*, 2017, **9**, 12355–12365.
154 H. Wu, W. Sun, J. Shen, C. Lu, Y. Wang, Z. Wang and K. Sun, *Nanoscale*, 2018, **10**, 13149–13158.
155 L. Zou, J. Cheng, Y. Jiang, Y. Gong, B. Chi, J. Pu and L. Jian, *RSC Adv.*, 2016, **6**, 31248–31255.
156 S. Ma, L. Sun, L. Cong, X. Gao, C. Yao, X. Guo, L. Tai, P. Mei, Y. Zeng, H. Xie and R. Wang, *J. Phys. Chem. C*, 2013, **117**, 25890–25897.
157 X. Cao, J. Wu, C. Jin, J. Tian, P. Strasser and R. Yang, *ACS Catal.*, 2015, **5**, 4890–4896.
158 X. Cao, Z. Sun, X. Zheng, J. Tian, C. Jin, R. Yang, F. Li, P. He and H. Zhou, *J. Mater. Chem. A*, 2017, **5**, 19991–19996.
159 X. Cao, Z. Sun, X. Zheng, C. Jin, J. Tian, X. Li and R. Yang, *ChemSusChem*, 2018, **11**, 574–579.
160 Z. Li, Y. Lv, Y. Yu, J. Yin, K. Song, B. Yang, L. Yuan and X. Hu, *J. Alloys Compd.*, 2020, **817**, 152736.
161 G. Karkera, S. G. Chandrappa and A. S. Prakash, *Chem.–Eur. J.*, 2018, **24**, 17303–17310.
162 H. Wang, Y. Yang, Y. Liang, G. Zheng, Y. Li, Y. Cui and H. Dai, *Energy Environ. Sci.*, 2012, **5**, 7931–7935.
163 J. G. Kim, Y. Kim, Y. Noh and W. B. Kim, *ChemSusChem*, 2015, **8**, 1752–1760.
164 F. Zhu, J. Zhang, B. Yang, X. Shi, C. Lu, J. Yin, Y. Yu and X. Hu, *J. Alloys Compd.*, 2018, **749**, 433–440.
165 T. Ishihara, K. Yokoe, T. Miyano and H. Kusaba, *Electrochim. Acta*, 2019, **300**, 455–460.
166 S. G. Chandrappa, P. Moni, G. Karkera and A. S. Prakash, *Nanoscale Adv.*, 2019, **1**, 2392–2399.
167 C. Shenghai, S. Liping, K. Fanhao, H. Lihua and Z. Hui, *J. Power Sources*, 2019, **430**, 25–31.
168 K.-N. Jung, S. M. Hwang, M.-S. Park, K. J. Kim, J.-G. Kim, S. X. Dou, J. H. Kim and J.-W. Lee, *Sci. Rep.*, 2015, **5**, 7665.
169 D. Bin, Z. Guo, A. G. Tamirat, Y. Ma, Y. Wang and Y. Xia, *Nanoscale*, 2017, **9**, 11148–11157.
170 Y. Kang, D. Zou, J. Zhang, F. Liang, K. Hayashi, H. Wang, D. Xue, K. Chen, K. R. Adair and X. Sun, *Electrochim. Acta*, 2017, **244**, 222–229.
171 Y. Liu, X. Chi, Q. Han, Y. Du, J. Huang, X. Lin and Y. Liu, *Nanoscale*, 2019, **11**, 5285–5294.
172 Y. Zhu, X. Liu, S. Jin, H. Chen, W. Lee, M. Liu and Y. Chen, *J. Mater. Chem. A*, 2019, **7**, 5875–5897.
173 F. Cheng and J. Chen, *Chem. Soc. Rev.*, 2012, **41**, 2172–2192.
174 M. Shao, Q. Chang, J.-P. Dodelet and R. Chenitz, *Chem. Rev.*, 2016, **116**, 3594–3657.
175 Y. Wang, Q. Cao, C. Guan and C. Cheng, *Small*, 2020, **16**, 2002902.
176 J. Han, J. Bian and C. Sun, *Research*, 2020, **2020**, 9512763.
177 T. Zhao, S. Gadipelli, G. He, M. J. Ward, D. Do, P. Zhang and Z. Guo, *Chemsuschem*, 2018, **11**, 1295–1304.
178 D. Yan, Y. Li, J. Huo, R. Chen, L. Dai and S. Wang, *Adv. Mater.*, 2017, **29**, 1606459.
179 N.-T. Suen, S.-F. Hung, Q. Quan, N. Zhang, Y.-J. Xu and H. M. Chen, *Chem. Soc. Rev.*, 2017, **46**, 337–365.

180 H. Yang, F. Hu, Y. Zhang, L. Shi and Q. Wang, *Nano Res.*, 2016, **9**, 207–213.
181 T. Y. Ma, Y. Zheng, S. Dai, M. Jaroniec and S. Z. Qiao, *J. Mater. Chem. A*, 2014, **2**, 8676–8682.
182 W. Wang, L. Kuai, W. Cao, M. Huttula, S. Ollikkala, T. Ahopelto, A.-P. Honkanen, S. Huotari, M. Yu and B. Geng, *Angew. Chem., Int. Ed.*, 2017, **56**, 14977–14981.
183 G. Fu, Z. Liu, J. Zhang, J. Wu, L. Xu, D. Sun, J. Zhang, Y. Tang and P. Chen, *Nano Res.*, 2016, **9**, 2110–2122.
184 P. W. Menezes, A. Indra, N. R. Sahraie, A. Bergmann, P. Strasser and M. Driess, *Chemsuschem*, 2015, **8**, 164–171.
185 T. Zhang, Z. Li, L. Wang, P. Sun, Z. Zhang and S. Wang, *Chemsuschem*, 2018, **11**, 2730–2736.
186 W. Fu, X.-L. Wang, X.-X. Yang and X.-Q. He, *ChemistrySelect*, 2018, **3**, 4228–4236.
187 X. He, F. Yin, S. Yuan, N. Liu and X. Huang, *Chemelectrochem*, 2016, **3**, 1107–1115.
188 Y. Liang, H. Wang, J. Zhou, Y. Li, J. Wang, T. Regier and H. Dai, *J. Am. Chem. Soc.*, 2012, **134**, 3517–3523.
189 X. Cao, C. Jin, F. Lu, Z. Yang, M. Shen and R. Yang, *J. Electrochem. Soc.*, 2014, **161**, H296–H300.
190 J. Shi, K. Lei, W. Sun, F. Li, F. Cheng and J. Chen, *Nano Res.*, 2017, **10**, 3836–3847.
191 X. Chen, R. Li, J. Wang, Q. Zhong and Y. Bu, *ChemistrySelect*, 2016, **1**, 2159–2162.
192 S. K. Singh, V. Kashyap, N. Manna, S. N. Bhange, R. Soni, R. Boukherroub, S. Szunerits and S. Kurungot, *ACS Catal.*, 2017, **7**, 6700–6710.
193 A. Ashok, A. Kumar, J. Ponraj and S. A. Mansour, *J. Electrochem. Soc.*, 2020, **167**, 054507.
194 X. Ge, Y. Liu, F. W. T. Goh, T. S. A. Hor, Y. Zong, P. Xiao, Z. Zhang, S. H. Lim, B. Li, X. Wang and Z. Liu, *ACS Appl. Mater. Interfaces*, 2014, **6**, 12684–12691.
195 A. Zhao, J. Masa, W. Xia, A. Maljusch, M.-G. Willinger, G. Clavel, K. Xie, R. Schlögl, W. Schuhmann and M. Muhler, *J. Am. Chem. Soc.*, 2014, **136**, 7551–7554.
196 Y. Yang, R. Zeng, Y. Xiong, F. J. DiSalvo and H. D. Abruña, *Chem. Mater.*, 2019, **31**, 9331–9337.
197 C. Xu, M. Lu, Y. Zhan and J. Y. Lee, *RSC Adv.*, 2014, **4**, 25089–25092.
198 X. Yan, Y. Jia, J. Chen, Z. Zhu and X. Yao, *Adv. Mater.*, 2016, **28**, 8771–8778.
199 D. Wang, X. Chen, D. G. Evans and W. Yang, *Nanoscale*, 2013, **5**, 5312–5315.
200 J. M. Gonçalves, M. Ireno da Silva, L. Angnes and K. Araki, *J. Mater. Chem. A*, 2020, **8**, 2171–2206.
201 C. Ye, M. Q. Wang, S. J. Bao and C. Ye, *ACS Appl. Mater. Interfaces*, 2019, **11**, 30887–30893.
202 L. Yu, H. Zhou, J. Sun, F. Qin, F. Yu, J. Bao, Y. Yu, S. Chen and Z. Ren, *Energy Environ. Sci.*, 2017, **10**, 1820–1827.
203 Y. Gong, Z. Xu, H. Pan, Y. Lin, Z. Yang and X. Du, *J. Mater. Chem. A*, 2018, **6**, 5098–5106.
204 J. M. Gonçalves, P. R. Martins, K. Araki and L. Angnes, *J. Mater. Chem. A*, 2020, **8**, 2171–2206.
205 S. Chu, H. Sun, G. Chen, Y. Chen, W. Zhou and Z. Shao, *ACS Appl. Mater. Interfaces*, 2019, **11**, 25227–25235.
206 Y.-J. Wang, H. Fan, A. Ignaszak, L. Zhang, S. Shao, D. P. Wilkinson and J. Zhang, *Chem. Eng. J.*, 2018, **348**, 416–437.
207 Y. Gong, Y. Lin, Z. Yang, F. Jiao, J. Li and W. Wang, *Appl. Surf. Sci.*, 2019, **476**, 840–849.
208 J. Zhang, X. Zhao, L. Du, Y. Li, L. Zhang, S. Liao, J. B. Goodenough and Z. Cui, *Nano Lett.*, 2019, **19**, 7457–7463.
209 J. Béjar, L. Álvarez-Contreras, J. Ledesma-García, N. Arjona and L. G. Arriaga, *J. Electroanal. Chem.*, 2019, **847**, 113190.
210 Y. Huang, W. Yang, Y. Yu and S. Hao, *J. Electroanal. Chem.*, 2019, **840**, 409–414.
211 A. Rebekah, E. Ashok Kumar, C. Viswanathan and N. Ponpandian, *Int. J. Hydrogen Energy*, 2020, **45**, 6391–6403.
212 A. Rebekah, S. Anantharaj, C. Viswanthan and N. Ponpandian, *Int. J. Hydrogen Energy*, 2020, **45**, 14713–14727.
213 X. Huang, H. Zheng, G. Lu, P. Wang, L. Xing, J. Wang and G. Wang, *ACS Sustainable Chem. Eng.*, 2019, **7**, 1169–1177.
214 R. Burch, *Phys. Chem. Chem. Phys.*, 2006, **8**, 5483–5500.
215 Y. Suchorski, R. Wrobel, S. Becker and H. Weiss, *J. Phys. Chem. C*, 2008, **112**, 20012–20017.
216 F. Yang, J. Graciani, J. Evans, P. Liu, J. Hrbek, J. F. Sanz and J. A. Rodriguez, *J. Am. Chem. Soc.*, 2011, **133**, 3444–3451.
217 X. Du, H. Su and X. Zhang, *Int. J. Hydrogen Energy*, 2019, **44**, 21637–21650.
218 C. Sun, J. Yang, Z. Dai, X. Wang, Y. Zhang, L. Li, P. Chen, W. Huang and X. Dong, *Nano Res.*, 2016, **9**, 1300–1309.
219 M. Liu, R. Zhang and W. Chen, *Chem. Rev.*, 2014, **114**, 5117–5160.
220 S. Hirai, S. Yagi, A. Seno, M. Fujioka, T. Ohno and T. Matsuda, *RSC Adv.*, 2016, **6**, 2019–2023.
221 J. Ge, W. Zhang, J. Tu, T. Xia, S. Chen and G. Xie, *Small*, 2020, **16**, 2001856.
222 J. Greeley, T. F. Jaramillo, J. Bonde, I. Chorkendorff and J. K. Nørskov, *Nat. Mater.*, 2006, **5**, 909–913.
223 K. Wang, X. She, S. Chen, H. Liu, D. Li, Y. Wang, H. Zhang, D. Yang and X. Yao, *J. Mater. Chem. A*, 2018, **6**, 5560–5565.
224 J. Han, S. Hao, Z. Liu, A. M. Asiri, X. Sun and Y. Xu, *Chem. Commun.*, 2018, **54**, 1077–1080.
225 J. Li, Y. Zhang, L. Li, Y. Wang, L. Zhang, B. Zhang, F. Wang, B. Li and X.-Y. Yu, *Dalton Trans.*, 2019, **48**, 17022–17028.
226 X. Du, J. Fu and X. Zhang, *CrystEngComm*, 2019, **21**, 7293–7302.
227 K. Lankauf, K. Cysewska, J. Karczewski, A. Mielewczyk-Gryń, K. Górnicka, G. Cempura, M. Chen, P. Jasiński and S. Molin, *Int. J. Hydrogen Energy*, 2020, **45**, 14867–14879.

